3.2. In-vivo testing of spectra measurement and analysis

An in-vivo experiment with a porcine brain was conducted to evaluate the accuracy of tumor identification (Fig. 12a). The target was the brain surface exposed by craniotomy under anesthesia. Spectra of the brain tissues were acquired in-vivo. The porcine received 20 mg/kg 5-ALA intravenously administering after induction of anaesthesia. The experiment commences in the usual fashion with resection of tumor portions, which were easily indentified under conventional white light illumination. A threshold was set for the intensity level of the measured fluorescence.

The tumor regions were detected using a two-dimensional histogram acquired from two sets of intensity images. The samples were evaluated through fluorescent measurement of brain tissues in-vivo. To reduce the effect of intrinsic fluorescence emanating from the tissue and other factors like blood flow, we also used two long pass filters (LPF) with cut-off wavelength of 550 and 610 nm to pass longer wavelengths over the active range. The optical filters were used to analyze the fluorescence spectra and to identify tumor and non-tumor areas more accurately. We constructed a feature space with the wavelength intensity in the range of 550–610 nm and a wavelength intensity of over 610 nm. K-means clustering (MacQueen, 1967) was used to calculate the barycentric coordinates of the two fluorescence intensities in the feature space. We set the barycentric coordinates to an initial value and derived each parameter of the mixture normal distribution with the Expectation–maximization (EM) algorithm (Dempster et al., 1977). A probability over 0.5 was regarded as the tumor. Fig. 12b shows the probability distributions for the area of the malignant and non-malignant glioma, which could be clearly discriminated. Regions in which fluorescent properties were detected were statistically analyzed.

3.3. System evaluation experiment

After finishing the fluorescence spectra analysis, we evaluated the system to confirm whether it can delineate the spatial boundary between the area with fluorescence and that without fluorescence with the guidance of MRI and fluorescence. We fabricated a container of 122 mm × 70 mm × 49 mm with a set of POLARIS markers attached along its circumference and placed a phantom (20 mm × 20 mm) inside it (Fig. 13a). The phantom was an agar plate containing a substance, Intralipid-10%, which is intravenous lipid emulsion used as a scattering medium. The concentration of the Intralipid-10% was adjusted to obtain an optimal scattering coefficient, one that was close to that of glioma. Half of the phantom contained PpIX, and the other half did not (Fig. 13a, upper right).

The rectangular area in Fig. 13a shows the area scanned by the system. The container was filled with water and scanned by MR. The MR image data for the phantom consisted of one set of coronal

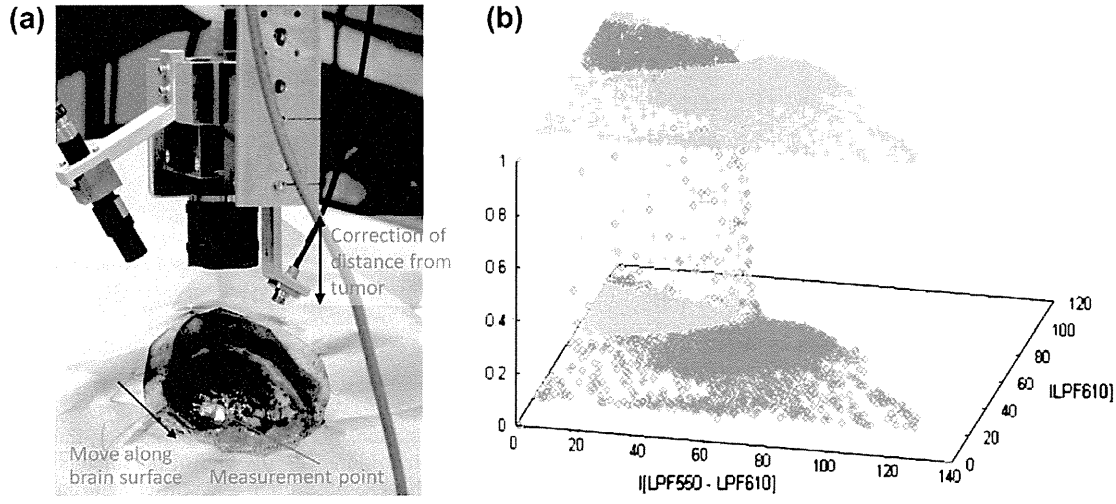

Fig. 12. (a) Experimental setup for in-vivo spectral measurement; (b) results of spectral analysis for malignant and non-malignant glioma.

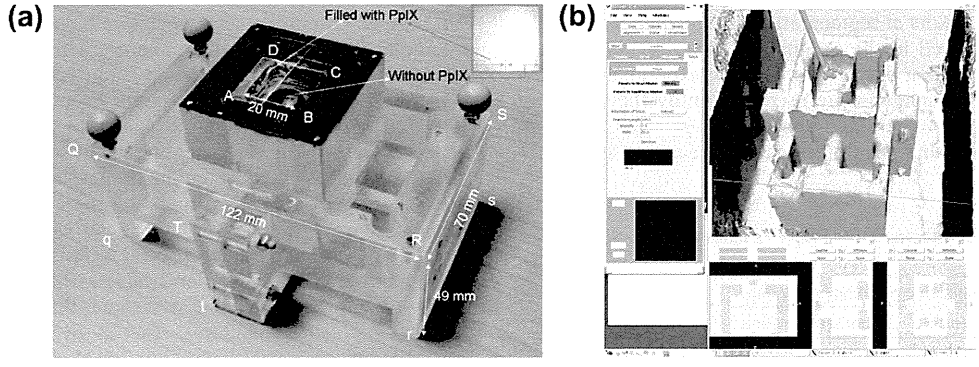

Fig. 13. Phantom for evaluation experiment: (a) Container with set of POLARIS markers attached along circumference and PpIX-filled agar phantom; (b) registration of PpIX fluorescence results with 3-D model generated from MRI.

images with a 1.0 × 1.0-mm in-plane resolution and a 1.0-mm slice thickness. Five points (Q, R, S, t, r) were used for image registration within the physical space of the phantom. Four points (A, B, C, D) were used for registration accuracy evaluation. The TRE for 100 tests of the four points was 1.79 ± 0.35 mm by comparing the coordinates of the MR images and corresponding measurement results with POLARIS optical tracking system (Table 2). The accuracy limitation for the phantom experiment relates to the optical tracking of the 3D-positions registration system and the scanned MR images. For surgical implementation or in-vivo experiments, deformation or movement of the tissue during the operation should also be considered. It took about several 100 ms to acquire the fluorescence and analyze its spectra for each scan and several minutes for scanning for a 10 × 10 mm area. Future work includes improving the scanning mechanism and shortening the procedure time.

We conducted another experiment to evaluate the MRI guided navigation system. The measured fluorescence spectra were integrated into the phantom model generated by MRI (Fig. 13b). The results showed that the system could delineate the spatial boundary between the area with fluorescence and that without fluorescence and that it could precisely ablate the fluorescent area with automatic scanning.

3.4. MRI-guided tumor identification with fluorescence

MR scanning was performed to image the 3-D structure of a brain (256 × 256 pixels, 128 slices, 1.0-mm thickness). Volumetric images and 3D models of the brain were reconstructed (Fig. 14a), and the results were combined with simulation information of 5-ALA-induced PpIX fluorescence (Fig. 14b). User interface of the integration system was developed as an extended module based on 3D Slicer (http://www.slicer.org/). The images were integrated in neurosurgery and displayed for guidance during laser ablation implementation, and the identified tumor area was photocoagulated by a scanning laser.

The fluorescence spectral analysis results were roughly mapped onto the MRI model so that we could move the microscope with the auto-focusing mechanism to the required area. The weak fluorescence signals in the boundary area could be strengthened by supplementation of MR information with further investigation on the precision registration. During treatment, the CCD images were used to determine the tumor area. After setting the surgical area, the ablation laser and fluorescence collection probe mounted on the microscope were controlled using the AF scanning mechanism.

Table 2
Results of the registration experiment.

	Coordinate in MR Image (mm)			Coordination measured by optical tracking system (mm)			Errors (mm)
	X	Y	Z	X	Y	Z	
A	10.1	33.1	9.4	10.6	34.6	10.8	2.11
B	10.1	33.3	−9.4	11.3	32.9	−8.7	1.41
C	−9.7	33.0	−10.1	−8.9	34.6	−10.8	1.92
D	−9.6	32.9	9.6	−9.1	33.8	11.0	1.72
R	34.6	12.0	−61.4	34.6	12.0	−61.4	0.0
r	34.5	−35.2	−60.9	34.5	−35.7	−60.9	0.5
S	−35.8	12.1	−61.5	−35.9	12.0	−61.5	0.2
Q	−34.2	12.5	−60.7	−34.2	12.5	−61.4	0.7
t	49.7	−33.7	9.7	49.7	−34.1	9.7	0.4

3.5. Laser ablation experiment

The laser scanning and ablation system were evaluated in-vivo using porcine brain tissue. Fluorescence detection and ablation laser probes were mounted on a non-contact surface-profiling microscope with an AF mechanism. The movement of the whole device was controlled with a medical robotic arm. A set of optical tracking markers were attached to the device for pre-operative navigation and thus for rough identification of tumor areas. The CCD camera was used to observe local information for the target area. The measurement area can thus be set in the CCD camera view with guidance from the navigation. During the operation, we also used local information like blood vessels and anatomic structures on the brain as landmarks and compared the outline on the brain with the target line for fluorescence detection and laser scanning. The in-vivo laser ablation experiment setup is shown in Fig. 15a, and the experimental scene is shown in Fig. 15b.

The wavelength of the laser was 2.8 mm, and the irradiation power was 0.36 W. The beam spot diameter was 0.16 mm, and the ablation speed was 3 mm/s. A medical doctor controlled the laser ablation after obtaining the spatial position information and corresponding fluorescence analysis results for the tumor. Fig. 16a shows an image of tumor tissue taken before laser ablation. After finishing the scanning test and fluorescence analysis, the laser ablation probe was guided to ablate the targeted tumor

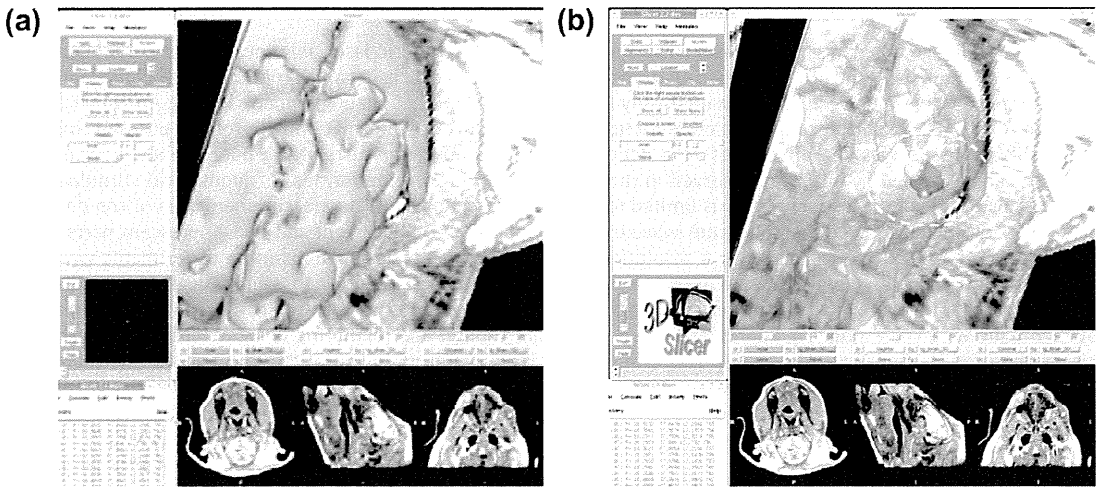

Fig. 14. Integration of fluorescence spectra with MRI model. (a) Reconstructed 3D models; (b) integration of fluorescence spectra.

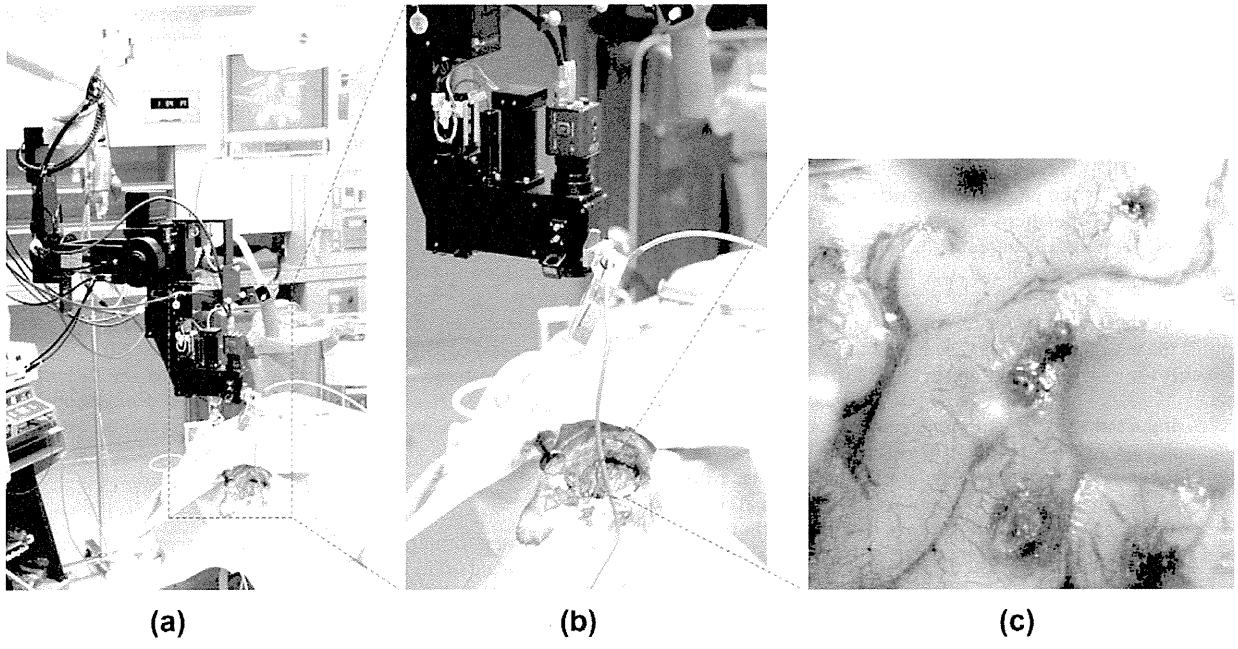

Fig. 15. (a) In-vivo laser scanning and ablation experiment setup; (b) surgical area; (c) experiment scene.

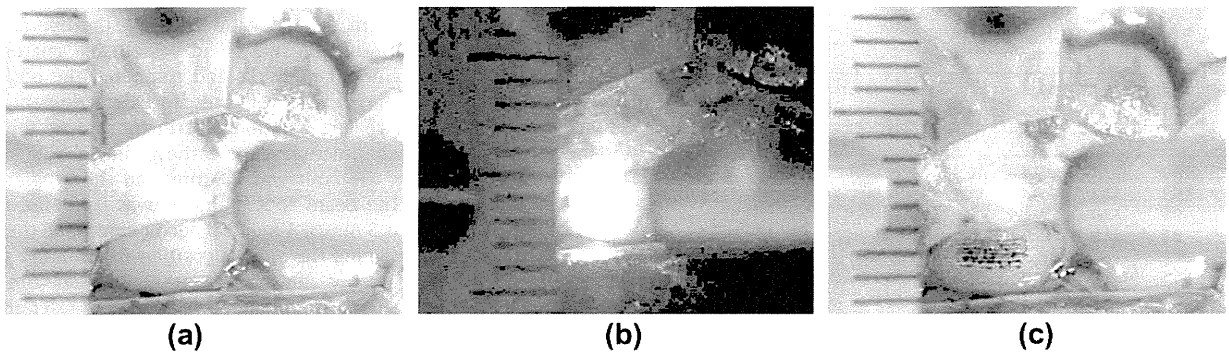

Fig. 16. In-vivo laser ablation experiment: (a) Before the laser ablation; (b) during laser photocoagulation; (c) after the laser ablation.

area. Fig. 16b shows an image taken after the ablation. Laser scanning of the surface of the brain with 0.1-mm spacing along the laser-scanned line showed that the tissue had been uniformly laser ablated, as shown in Fig. 16c. We also examined a cross section of the tissue. The ablated tissue was sharply incised to a depth of about 0.5 mm. No change caused by heat was observed in the tissue, meaning that absorption of the laser energy was limited to the brain surface. The experiments showed that a 2.8-mm-wavelength micro-laser can form an ablated incised lesion at a resolution of 0.1 mm or less without thermally damaging surrounding tissue.

These results show that the developed intra-operative diagnosis and therapy technique with corresponding fluorescence detection and analysis can be used to identify a tumor area and that laser ablation is a valid treatment for the surface of a target tumor.

4. Discussion

We developed a computer-aided navigation system using 5-ALA-induced PpIX fluorescence and 3-D MRI anatomical structure data for robotic laser ablation of tumor. The ablation system has automatic focusing and a robotic scanning mechanism and was designed for malignant glioma treatment. Ablation is performed using fluorescence information with robotic position control.

Combination tests of the fluorescence measurement and laser ablation were performed for biomedical stimulant phantoms and a porcine brain. The measurement area of the phantoms was separated into fluorescent and non-fluorescent parts. The preliminary nature of the designed phantom experiments was to indentify the fluorescence intensity threshold, discriminate the fluorescent region, and determine the distribution of the fluorescence intensity. Although the phantoms designs were simple and differed from those of in-vivo brain and tumor tissues, it was possible to identify the fluorescent area accurately from the spectral data. The discrimination error at the boundary line was within 0.1 mm. The identified area was selectively ablated by automatic scanning with the micro ablation laser. For even higher-precision evaluation, the phantoms should be redesigned and to overcome the limitations. A multi-layer phantom or a mixed phantom carrying embedded

fluorophores, chromophores, and scatterers with adequate optical parameters like absorption and fluorescence emission (Chernova et al., 1998) could be used to simulate tissues more accurately. The predominant species used for modeling tissue include the reduced form of nicotinamide adenine dinucleotide (NADH) (Lakowicz, 1985) and the various flavins (FAD, etc.) (Masters et al., 1993) with dominant fluorophores in the tissue. Compared with using phantoms, a combination of local spectrum measurement for in-vivo tissue and corresponding microscope-based pathological analysis is a more practical approach to improving the accuracy of fluorescent intensity threshold identification and fluorescent region discrimination.

In clinical cases, the boundaries between tumors and normal tissue are often unclear, and parts of a tumor can extend into normal tissue, so a simple thresholding method is not well suited to treatment around the boundaries. For example, it may be necessary to cluster the areas containing gray-matter. Therefore, deciding the threshold for the fluorescence data and identifying the area to be ablated are challenging. We are thus developing a system with improved measurement accuracy that can better handle complicated tumor tissue structures. To enable the combined tumor region to be automatically discriminated by using fluorescence spectra, we will investigate a multiple classification analysis based on other spectral features as well as the peak intensity of the fluorescence. This system will also combine automatic processing with robotic laser ablation.

The MRI navigation is used to roughly identify the position of the tumor. The phantom experiment produced both types of image data for the simulated tumor and its boundaries, and the fluorescence data can be integrated into the MRI data after registration. A previous in-vivo experiment using both types of image data demonstrated the correlation between regions with and without fluorescence (Aoki et al., 2007). However, our experiments only demonstrated the use of the AF device mounted on a robotic manipulator. In the in-vivo experiment, scanning and laser ablation were performed on the brain surface. A more difficult challenge is focusing the laser beam on the vertical portions of the brain's curved surfaces, especially on the side of a tumor. Actually, for a sharp or curved surface, it would be better if we could adjust the normal direction of the probe to perform the laser ablation more effectively. We plan to develop a smaller device that can be controlled more flexibly for adjusting the direction of the probe to match a curved surface. Furthermore, our future work includes the development of a hand-held device that combines fluorescence acquirement and laser ablation. Used instead of a microscope, it would be installed into an endoscope for use in resection of brain tumors located in deep areas.

With our current system, the entire tumor is first scanned and the tumor area is indentified. Laser ablation is performed after fluorescence spectral analysis. Since deformation and movement of the brain tissue occurs during the procedure, our next-generation system will combine the spectral analysis and laser ablation to enable diagnosis and therapy to be done simultaneously. Although both the scanning and AF servo-mechanisms have a precision of 10 μm, which is enough to ensure the accuracy of the area to be ablated even in the presence of small tissue deformation in the target area, the scanning and spectral analysis speeds should be increased. For fluorescence diagnosis to be integrated with laser ablation therapy, the fluorescence spectral analysis and tumor identification accuracies should be enhanced. Furthermore, temporal response of 5-ALA-induced fluorescence should also be considered, especially for tracking small or deformed targets. The temporal information could be incorporated into the segmentation framework to further enhance the accuracy of the proposed technique.

As mentioned above, it was difficult to discriminate the PpIX area by simply using the luminance threshold whereas the area containing PpIX solution was clearly discriminated by simply using the spectral intensity level. This is because the luminance thresholding could not discriminate the fluorescence from the background reflection light of the highly scattering surface (even in a dark room); in our experiment, the scattering factor of the non-PpIX area was ten times that of the PpIX area. Since the reflectance property depends on not only the scattering factor but also the target's inclination and undulation, we speculate that, as compared with the discrimination using a camera and optical filters, discrimination using spectral data works more effectively for brain tissue, which has much undulation and is composed of several kinds of tissue with different optical properties. Our future work includes the development of more sophisticated processes that would provide better discrimination for the luminance thresholding.

Although high grade gliomas are easier to recognize than low grade ones, how to identify complex areas (such as a tumor combined with surrounding blood vessels) and small tumors is still difficult. Development of fluorescence identification materials (fluorescence markers) for low grade gliomas is also important. Furthermore, the fluorescence markers should be improved to enable the material to be ingested by all tumor cells and the fluorescence to be completely identified.

5. Conclusion

We have developed an integrated diagnosis and therapeutic system for precision neurosurgery, and given a proof of concept for the integration of diagnostic and therapeutic techniques. The system combines tumor detection using 5-ALA-induced PpIX fluorescence and precise ablation using a micro-laser with an automatic focusing and robotic mechanism for scanning the brain surface. In this study, the areas of the experimental targets with and without fluorescence were clearly discriminated. Ablation is performed using fluorescent information and robotic position control. The measurement area is sectioned into a grid pattern and measurement is performed at the central point in each square using scanning. The fluorescence intensity is calculated from the spectral data, and the area is binarized using thresholding method and the regions of fluorescent properties are statistically analyzed. A target area is selectively irradiated with the micro ablation laser. The experimental results showed that the system can identify the regions with fluorescence appropriately from the measurement data and that the ablation system can be automatically guided by the navigation system.

Compared with discrimination using a camera and optical filters, discrimination using spectral analysis is affected less by the reflectance properties of the targets, which depend on the scattering factor and the target's geometry, so it is more effective for brain tissue, which has much undulation and is composed of several kinds of tissue with different optical properties.

Acknowledgments

This work was supported in part by Grant for Translational Systems Biology and Medicine Initiative (TSBMI) from the Ministry of Education, Culture, Sports, Science and Technology of Japan. H. Liao was also supported by Grant for Industrial Technology Research of New Energy and Industrial Technology Development Organization, Japan, and Grant-in-Aid for Scientific Research of the Japan Society for the Promotion of Science. We thank Koji Shimaya and Kaimeng Wang for their helps in experiment and data collection.

References

Ando T., Noguchi M., Kobayashi E., Liao H., Maruyama T., Muragaki Y., Iseki H., Sakuma I., 2009. Local Spectrum measurement system for 5-Aminolaevulinic

acid Induced Protoporphyrin IX fluorescence. In: World Congress on Medical Physics and Biomedical Engineering, Munich, Germany, September 7–12, 2009; IFMBE Proceedings 25/II, 375-378.
Aoki, E., Noguchi, M., Hong, J.S., Kobayashi, E., Nakamura, R., Maruyama, T., Muragaki, Y., Iseki, H., Sakuma, I., 2007. Development of an intraoperative information integration system and implementation for neurosurgery. Journal of Robotics and Mechatronics 19 (3), 339–352.
Chernova, S.P., Pravdin, A.B., Sinichkin, Y.P., Tuchin, V.V., Vari, S.G., 1998. Physical modeling of tissue fluorescence. phantom development, EUROPTO Conference on Optical Biopsy, Optical Biopsies and Microscopic Techniques III. SPIE 3568, 66–71.
Clatz, O., Delingette, H., Talos, I.F., Golby, A.J., Kikinis, R., Jolesz, F.A., Ayache, N., Warfield, S.K., 2005. Robust nonrigid registration to capture brain shift from intraoperative MRI. IEEE Transactions on Medical Imaging 24 (11), 1417–1427.
Ciburis, A., Gadonas, D., Didziapetriene, J., et al., 2003. 5-Aminolevulinic acid induced protoporphyrin IX fluorescence for detection of brain tumor cells in vivo. Experimental Oncology 25 (1), 51–54.
Cohen, D., 1968. Magnetoencephalography: evidence of magnetic fields produced by alpha rhythm currents. Science 161, 784–786.
Dempster, A.P., Laird, N.M., Rubin, D.B., 1977. Maximum likelihood from incomplete data via the EM algorithm. Journal of the Royal Statistical Society. Series B (Methodological) 39 (1), 1–38.
Fukaya, C., Katayama, Y., Murata, Y., Kobayashi, K., Kasai, M., Yamamoto, T., Sakatani, K., 2002. Localization of eloquent area utilize to functional MRI in patients with brain tumor. International Congress Series 1232, 763–767.
Gholipour, A., Kehtarnavaz, N., Briggs, R., Devous, M., Gopinath, K., 2007. Brain functional localization: a survey of image registration techniques. IEEE Transactions on Medical Imaging 26 (4), 427–451.
Hashizume, A., Shrestha, P., et al., 2007. Functional brain mapping and localizing epileptic zone with magnetoencephalography: a review of two cases with illustrations. Nepal Journal of Neuroscience 4, 106–109.
Hirai, N., Kosaka, A., Kawamata, T., Hori, T., Iseki, H., 2005. Image-guided neurosurgery system integrating AR-based navigation and open-MRI monitoring. Computer Aided Surgery 10 (2), 59–71.
Keles, G.E., Lundin, D.A., Lamborn, K.R., Chang, E.F., Ojemann, G., Berger, M.S., 2004. Intraoperative subcortical stimulation mapping for hemispherical perirolandic gliomas located within or adjacent to the descending motor pathways: evaluation of morbidity and assessment of functional outcome in 294 patients. Journal of Neurosurgery 100 (3), 369–375.
Lakowicz, J.R., 1985. Principles of Fluorescent Spectroscopy. Plenum Press.
Leblond, F., Fontaine, K.M., Valdes, P., Ji, S., Pogue, B.W., Hartov, A., Roberts, D.W., Paulsen, K.D., 2009. Brain tumor resection guided by fluorescence imaging. In: Kessel, David H. (Ed.), Optical Methods for Tumor Treatment and Detection: Mechanisms and Techniques in Photodynamic Therapy XVIII, vol. 7164. Proc SPIE.
Liao, H., Inomata, T., Sakuma, I., Dohi, T., 2006. Surgical navigation of Integral Videography image overlay for open MRI-guided glioma surgery. The 3rd International Workshop on Medical Imaging, Augmented Reality, MIAR. Lecture Notes in Computer Science. LNCS 4091, 187–194.
Liao, H., Noguchi, M., Maruyama, T., Muragaki, Y., Iseki, H., Kobayashi, E., Sakuma, I., 2010. Automatic focusing and robotic scanning mechanism for precision laser ablation in neurosurgery. In: The 2010 IEEE/RSJ International Conference on Intelligent Robots and System. IROS, pp. 325–330.
Liao, H., Shimaya, K., Wang, K., Maruyama, T., Noguchi, M., Muragaki, Y., Kobayashi, E., Iseki, H., Sakuma, I., 2008. Combination of Intraoperative 5-Aminolevulinic Acid-Induced Fluorescence, 3-D MR Imaging for Guidance of Robotic Laser Ablation for Precision Neurosurgery. 11th International Conference on Medical Image Computing, Computer-Assisted Intervention–MICCAI. Lecture Notes in Computer Science. LNCS 5242, 373–380.
MacQueen J. B., 1967. Some Methods for classification and Analysis of Multivariate Observations. In: Proceedings of 5th Berkeley Symposium on Mathematical Statistics and Probability, vol. 1. University of California Press, pp. 281–297.
Maruyama, T., Muragaki, Y., Iseki, H., Kubo, O., Mochizuki, M., Seo, S., Sakuma, I., Hori, T., Takakura, K., 2001. Intraoperative detection of malignant gliomas using 5-Aminolevulinic acid induced protoporphyrin fluorescence, open MRI and real-time navigation system, computer assisted radiology and surgery. International Congress Series 1230, 281–286.
Masters, B.R., Chance, B., 1993. In Fluorescent and Luminescent Probes for Biological Activity. In: Maon, W.T. (Ed.), Academic Press, London, p. 44.
Muragaki, Y., Kawamata, T., Iseki, H., Kubo, O., Maruyama, T., Amano, K., Hori, T., Takakura, K., 2001. New system of glioma removal using intraoperative MRI combined with functional mapping. Proceeding of Computer Assisted Radiology and Surgery 2001, 1143.
Noguchi, M., Aoki, E., et al., 2006. A Novel Robotic Laser Ablation System for Precision Neurosurgery with Intraoperative 5-ALA-Induced PpIX Fluorescence Detection". 9th International Conference on Medical Image Computing and Computer-Assisted Intervention–MICCAI 2006. LNCS 4190, 543–550.
Ogawa, S., Lee, T.M., Kay, A.R., Tank, D.W., 1990. Brain magnetic resonance imaging with contrast dependent on blood oxygenation. Proceedings of the National Academy of Science 87 (24), 9868–9872.
Omori, S., Muragaki, Y., Sakuma, I., Iseki, H., 2004. Robotic laser surgery with $\lambda = 2.8$ μm microlaser in neurosurgery. Journal of Robtics and Mechatronics 16 (2), 122–128.
Otsu, N., 1979. A threshold selection method from gray-level histograms. IEEE Transactions on Systems, Man, and Cybernetics 9, 62–66.
Pouratian, N., Cannestra, A.F., Bookheimer, S.Y., Martin, N.A., Toga, A.W., 2004. Variability of intraoperative electrocortical stimulation mapping parameters across and within individuals. Journal of Neurosurgery 101, 458–466.
Regula, J., MacRobert, A.J., Gorchein, A., et al., 1995. Photosensitisation and photodynamic therapy of oesophageal, duodenal, and colorectal tumours using 5-aminolaevulinic acid induced protoporphyrin IX-a pilot study. Gut 36, 67–75.
Rossi, F.M. et al., 1996. In vitro studies on the potential use of 5-aminolevulinic acid mediated photodynamic therapy for gynaecological tumors. British Journal of Cancer 74, 881–887.
Sosna, J., Barth, M.M., Kruskal, J.B., Kane, R.A., 2005. Intraoperative Sonography for Neurosurgery. Journal of Ultrasound in Medicine 24, 1671–1682.
Staveren, J., van Moes, J.M., Marle, J., van Prahl, A., Van Germert, J.C., 1991. Light scattering in Intralipid-10% in the wavelength range of 400–1100 nm. Applied Optics 30, 4507–4514.
Sterenborg, H.J. et al., 1989. The spectral dependence of the optical properties of the human brain. Lasers in Medical Science 4, 221–227.
Stummer, W., Novotny, A., Stepp, H., Goetz, C., Bise, K., Reulen, H.J., 2000. Fluorescence-guided resection of glioblastoma multiforme by using 5-aminolevulinic acid-induced porphyrins: a prospective study in 52 consecutive patients. Journal of Neurosurgery 93 (6), 1003–1013.
Stummer, W., Stepp, H., Möller, G., Ehrhardt, A., Leonhard, M., Reulen, H.J., 1998a. Technical principles for protoporphyrin-IX-fluorescence guided microsurgical resection of malignant glioma tissue. Acta Neurochirurgica 140 (10), 995–1000.
Stummer, W., Stocker, S., Wagner, S., Stepp, H., Fritsch, C., Goetz, C., Goetz, A.E., Kiefmann, R., Reulen, H.J., 1998b. Intraoperative detection of malignant gliomas by 5-aminolevulinic acid-induced porphyrin fluorescence. Neurosurgery 42, 518–525.
Suess, O., Suess, S., Brock, M., Kombos, T., 2006. Intraoperative electrocortical stimulation of Brodman area 4: a 10-year analysis of 255 cases. Head & Face Medicine 2, 20.
Unsgaard, G., Rygh, O.M., Selbekk, T., Muller, T.B., Kolstad, F., Lindseth, F., Nagelhus Hernes, T.A., 2006. Intra-operative 3D ultrasound in neurosurgery. Acta Neurochiurgica 148 (3), 235–253.
Valdes, P., Harris, B.T., Leblond, F., Fontaine, K.M., Ji, S., Pogue, B.W., Hartov, A., Roberts, D.W., Paulsen, K.D., 2009. Brain tumor resection guided by fluorescence imaging co-registered with MRI. In Proc. SPIE, 7261.
Vo-Dinh, T., 2003. Biomedical Photonics Handbook, CRC Press.

Int J CARS (2012) 7:931–939
DOI 10.1007/s11548-012-0743-0

ORIGINAL ARTICLE

A fluorolaser navigation system to guide linear surgical tool insertion

Jack T. Liang · Takehito Doke · Shinya Onogi · Satoru Ohashi · Isao Ohnishi · Ichiro Sakuma · Yoshikazu Nakajima

Received: 10 January 2012 / Accepted: 25 April 2012 / Published online: 25 May 2012

Abstract
Purpose Conventional navigation systems for minimally invasive orthopedic surgery require a secondary monitor to display guidance information generated with CT or MRI images. Newer systems use augmented reality to project surgical plans into binocular glasses. These surgical procedures are often mentally challenging and cumbersome to perform.
Method A comprehensive surgical navigation system for direct guidance while minimizing radiation exposure was designed and built. System accuracy was evaluated using in vitro needle insertion experiments. The fluoroscopic-based navigation technique is combined with an existing laser guidance technique. As a result, the combined system is capable of surgical planning using two or more X-ray images rather than CT or MRI scans. Guidance information is directly projected onto the patient using two laser beams and not via a secondary monitor.
Results We performed 15 in vitro needle insertion experiments as well as 6 phantom pedicle screw insertion experiments to validate navigation system accuracy. The planning accuracy of the system was found to be 2.32 mm and 2.28°, while its overall guidance accuracy was found to be 2.40 mm and 2.39°. System feasibility was demonstrated by successfully performing percutaneous pin insertion on phantoms.
Conclusion Quantitative and qualitative evaluations of the fluorolaser navigation system show that it can support accurate guidance and intuitive surgical tool insertion procedures without preoperative 3D image volumes and registration processes.

Keywords Percutaneous surgery · Orthopedic surgery · Laser guidance · Fluoroscopic navigation · Computer-aided surgery · Surgical navigation

J. T. Liang (✉) · T. Doke · I. Sakuma · Y. Nakajima
Graduate School of Engineering, The University of Tokyo,
Hongo 7-3-1, Bunkyo-ku, Tokyo 113-8656, Japan
e-mail: jliang@image.t.u-tokyo.ac.jp

S. Onogi · Y. Nakajima
Intelligent Modeling Laboratory, The University of Tokyo,
Hongo 7-3-1, Bunkyo-ku, Tokyo 113-8656, Japan

Y. Nakajima
e-mail: nakajima@bioeng.t.u-tokyo.ac.jp

S. Ohashi · I. Ohnishi
Graduate School of Medicine, The University of Tokyo,
Hongo 7-3-1, Bunkyo-ku, Tokyo 113-8654, Japan

Introduction

Percutaneous surgical interventions are widely accepted as they induce less damage on the patient's body compared to traditional open techniques. Visual access of the interior of the patient's body during orthopedic percutaneous procedures is possible with the use of medical imagining techniques such as X-ray computed tomography (CT), magnetic resonance (MR), and X-ray fluoroscopes. Captured imaging data are then processed by image-based surgical assistive systems, which can be divided into two functional systems: surgical navigation and surgical execution. Taking medical images as inputs, surgical navigation systems output processed data for use in the actual execution of surgeries. Schlenzka et al. [1] have classified navigation systems into three categories: passive navigators, active navigators, and semi-active navigators.

Conventional passive surgical navigation systems for orthopedic percutaneous surgeries offer information on where surgical insertions are to be made via an external monitor. However, the diversion of surgeon's attention and sight away from the patient results in lack of intuitiveness and reduced patient attention. This causes error and increases

surgical time. For viewing of surgical plans directly on the patient, recent systems adopt the use of augmented reality techniques. These systems include video see-through binocular systems [2], half-mirror display devices [3–5], direct image projectors [6,7], and single-laser beam pointers [8–13]. Drawbacks of the binocular and half-mirror devices include reduced visibility and increased sterilization. In the single-laser beam method, guidance is unstable when surface deformation occurs. Gavaghan et al. have proposed a display system [7] that is compact, nonobstructive, and can be easily integrated into existing navigation systems. It indicates needle insertion point, insertion orientation, and insertion depth via images projected onto the patient's body. However, specialized surgical tools are required when using this system.

The laser guidance system initially proposed by Sasama et al. [14] and later described by Nakajima et al. [15] is a passive navigator that uses X-ray CT images to guide surgical tool in orthopedic percutaneous surgeries. It has been specifically developed to guide the insertion of linear surgical tools during orthopedic interventions. It uses two laser beams to accurately display the insertion point and orientation directly on the patient's skin. Compared to existing navigation systems, this method is advantageous because it is robust toward surface deformations, does not require a secondary display panel, and does not require tracking of surgical tools. However, its surgical planning function requires the use of preoperatively captured X-ray CT data. As well, intraoperative 2D/3D registration of patient location using X-ray images is required to obtain real-world position coordinates. These steps increase the overall operational time, operation complexity, and radiation exposure for patients and medical personnel.

Alternative imaging techniques are necessary to address these problems. For instance, MR may be suitable as it can provide a highly accurate 3D visualization of the patient's tissues. However, it does not provide high resolution of bone intensity and is only suitable in nonmetal-containing environments, thus limiting the applicable patient populations. Traditional fluoroscopy can provide accurate, real-time intraoperative 2D views of patient anatomy. Conversely, its limitations include increased radiation exposure and difficulties in obtaining and processing multi-planar visualization.

In this paper, we present an improved navigation system that uses binary laser sources to guide surgical tool insertion using surgical plans drawn onto three intraoperatively taken fluoroscopic X-ray images. In particular, we supplanted the CT-based surgical planning procedure of the existing laser guidance system with that of the virtual fluoroscopy technique, which uses one or more fluoroscopic X-ray images for surgical planning [16,17]. Compared to CT imaging and conventional fluoroscopy, the virtual fluoroscopy technique does not require the usage of preoperative 3D models nor does it continuously expose surgeons and patients to X-ray radiation. Depending on the hardware utilized and surgical procedure, radiation exposure from a complete CT scan of the torso is roughly 1 Rem [18]. Radiation exposures for spine surgeries performed using traditional fluoroscopy versus virtual fluoroscopy were 4.33 and 0.33 mRem, respectively [19].

As far as the authors know, this is the first study to integrate the virtual fluoroscopic surgical planning technique with the dual-laser guidance technique. This novel combination yields an original passive surgical navigation and guidance system that displays tool insertion path directly in the surgical field without use of any presurgical techniques. Surgical plans are drawn onto 2D X-ray images and displayed via dual-laser beams.

Materials and methods

The proposed fluoroscopic-based dual-laser-guided fluorolaser navigation system combines the strength of fluoroscope-based navigation and laser guidance technique. This system consists of three major components: a Laser Guidance System [14,20,21] with the commercially available hybrid Polaris Spectra (Northern Digital, Waterloo, Canada) built-in, active infrared markers (AdapTrax 15 Marker, Northern Digital, Waterloo, Canada), and a fluoroscopic C-arm (Arcadis Orbic 3D, Siemens, Munich, Germany) used to capture 2D X-ray images. Accuracy of Polaris Spectra is 0.35 mm RMS within its working volume.

We implemented the fluorolaser software in C++ (Visual Studio 2005, Microsoft co.) with OpenCV library to obtain 2D images from the fluoroscopic C-arm. It connects to the laser guidance system over TCP/IP, to the Polaris tracking device via RS-232c, and to the fluoroscopic C-arm via a video output to USB converter. In this section, we will discuss the two functional parts of this new system, guiding and planning, as well as the experimental procedures.

Insertion guidance using lasers

The planned surgical tool insertion pathway is shown three-dimensionally by the intersection of two emitted laser beam planes. On any 2D surface, the binary lasers create two lines and one intersection point. The lasers simultaneously guide surgical tool's insertion point and its insertion orientation as shown in Fig. 1. The intersectional line L_0 made by laser planes S_1 and S_2 represents the insertion path in 3D space. The insertion point P_0 is the intersection of L_0 and the patient's body surface S_0. Insertion point guidance is robust to deformations of the body surface, represented by changes from S_0 to S_0' in Fig. 1. Surface S_0' represents any deviations from S_0 in both height and shape due to body surface relocation, deformation, or obstruction by soft tissues.

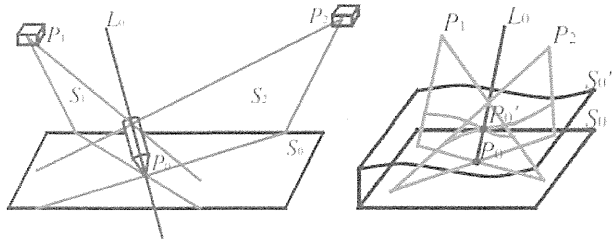

Fig. 1 *Left* schematic diagram of the laser guidance method. *Right* robust entry point displayed for surface relocation, deformation, or occlusion by soft tissue using dual-laser beams

For proper surgical tool alignment, the tip of the surgical tool is placed at P_0 and the length aligned to L_0. Orientation alignment can be verified using the projections of the lasers on the side of surgical tools. Proper alignment is indicated by two parallel lasers. A detailed description of this binary laser-emitting device is described by Nakajima et al. [15].

Navigational planning

Infrared markers are placed on the C-arm and the patient for tracking. Each infrared marker provides a 4-by-4 transformation matrix describing the rotation and translation displacement of the marker from the localizer origin. Thus, we can virtually construct an origin at the C-arm (CS_F) and the patient (CS_S) markers using transformations T_{fluoro} and $T_{subject}$, respectively (Fig. 2). The surgical planning process requires multiple sets of inputs. Each set consists of three pieces of information obtained from the surgical environment: a 2D X-ray image, T_{fluoro}, and $T_{subject}$. The X-ray image is obtained by the C-arm and must contain the surgical insertion site. The two transformations, T_{fluoro} and $T_{subject}$, are recorded when the X-ray image is taken. As shown in Fig. 2, a 2D surgical tool insertion path is manually drawn onto each acquired X-ray image, *Plan 1 and Plan 2*. This insertion path includes a point (P_i) and a vector (u_i), where the vector indicates the insertion orientation. The point can denote either one of two points on the same path: the insertion

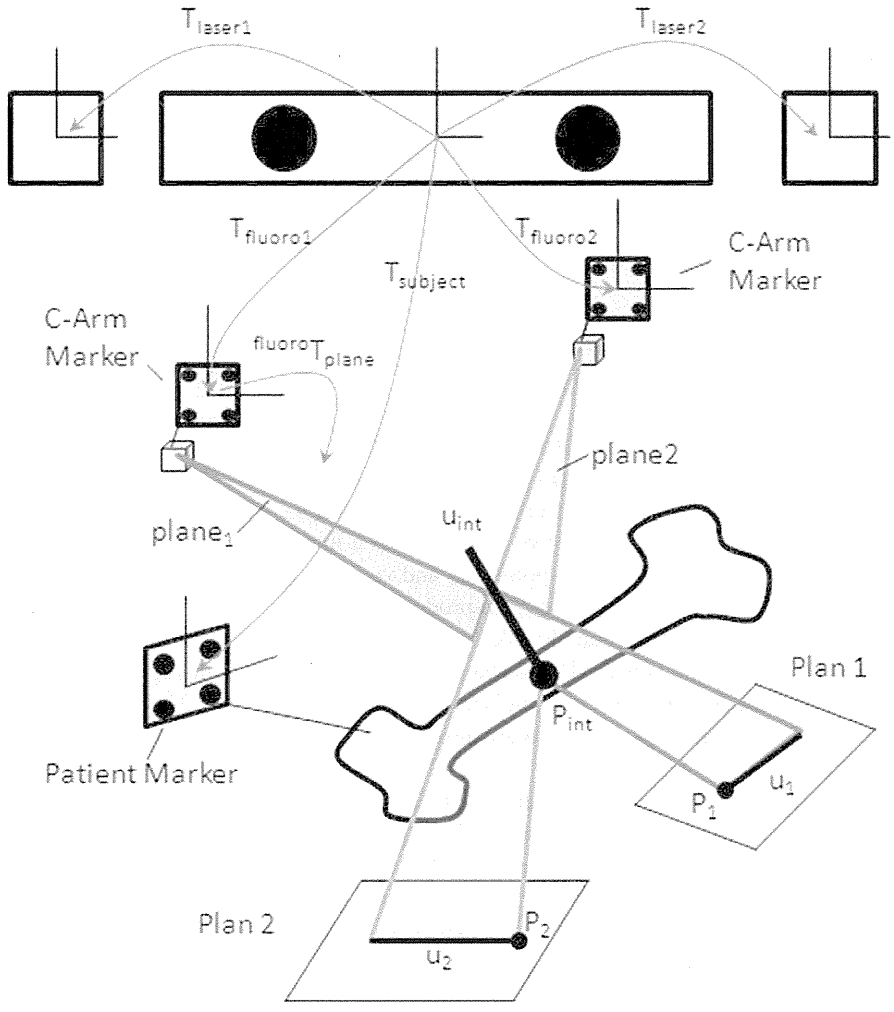

Fig. 2 Infrared markers are placed on the patient and C-arm. Transformation matrices include localizer to laser sources (T_{laser1} and T_{laser2}), localizer to subject ($T_{subject}$), and localizer to C-arm ($T_{fluoro1}$ and $T_{fluoro2}$). C-arm is positioned at two arbitrary locations. Using the appropriate ${}^{fluoro}T_{plane}$, surgical plans $\{P_1, u_1\}$ and $\{P_2, u_2\}$ on Plan 1 and Plan 2 are projected into $plane_1$ and $plane_2$, respectively, to calculate insertion path $\{P_{int}, u_{int}\}$ in 3D space

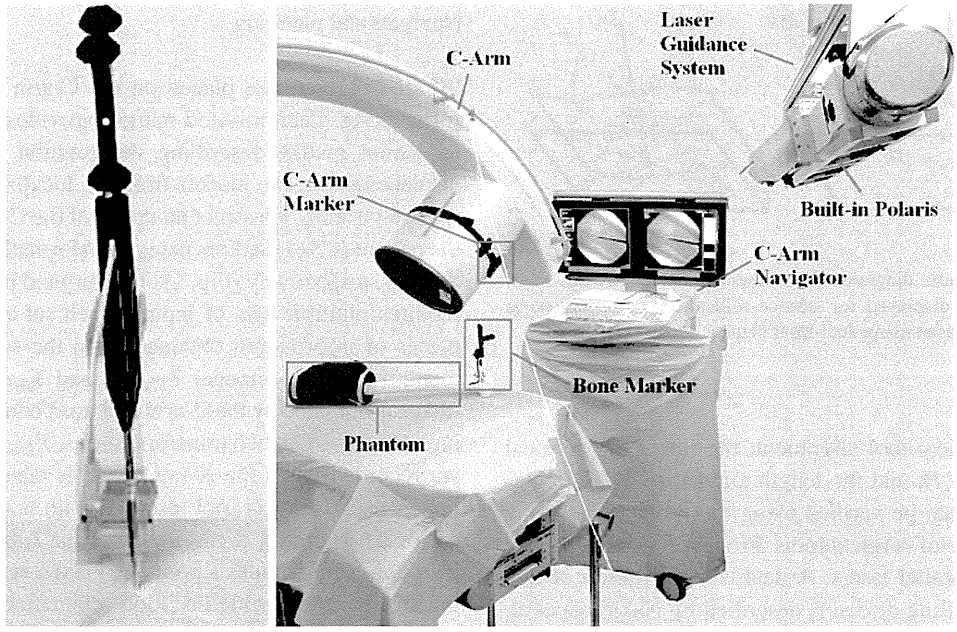

Fig. 3 *Left* proper orientation alignment is shown by parallel lasers on the side face of the linear wire with infrared marker and sleeve attached. *Right* experimental setup includes the laser guidance system with built-in optical tracking capabilities, a flat surface, a fluoroscopic C-arm, and a phantom. Infrared markers are used to locate the C-arm and phantom

point on the body surface or a target point inside the body. Using calibrated C-arm parameters described in the C-arm calibration section, this 2D plan is projected starting from the imaging device's pinhole and along its ray-lines to obtain a plane with normal vector n_i in 3D space. This plane is formulated in CS_F (Eq. 1) and transformed for use in CS_S (Eq. 2)

$$^{fluoro}T_{plane} = f_1\left(T_{calibration}, T_{plan2D}\right) \quad (1)$$

$$^{subject}T_{plane} = {T_{subject}}^{-1}\,{}^{fluoro}T_{fluoro}\,{}^{fluoro}T_{plane} \quad (2)$$

Following Fig. 2, two 2D plans from two sets of inputs yield two planes, $plane_1$ and $plane_2$, in the 3D navigation space. The normal vectors of $plane_1$ and $plane_2$ are n_1 and n_2, respectively. The intersection of two planes yields a line in 3D space and is described by the point P_{int} and vector u_{int}. The directional vector, u_{int}, is the cross products of n_1 and n_2. The point P_{int} in 3D space is calculated by projecting points P_1 and P_2 into lines in 3D space and finding the point at which these projected lines traverse. This intersection line described by P_{int} and u_{int} represents the insertion path in 3D space.

If three sets of inputs are used, three 2D plans are made to give three planes in 3D space. This gives rise to three very similar intersection lines in 3D space with 3D points $\{P_{int1}, P_{int2}, P_{int3}\}$ and 3D directional vectors $\{u_{int1}, u_{int2}, u_{int3}\}$. Simple algebraic regression of these three lines is performed to obtain a line of best fit. A circle is fitted to P_{int1}, P_{int2}, and P_{int3}. We define P_{reg} as the center of this circle. Vector averaging of u_{int1}, u_{int2}, and u_{int3} yields u_{reg}. The regressed line represents the optimal tool insertion path (Eq. 3). This optimal insertion path is expressed by $^{subject}T_{plan3D}$ and stored in CS_S. Thus, it is robust toward any movements of the surgical object. The z-axis of the matrix corresponds to u_{reg}. Following Eq. (4), $^{subject}T_{plan3D}$ is transformed from CS_S into the localizer-laser coordinate systems. Next, this insertion path is projected by the laser sources. Finally, surgical navigation by laser guidance is achieved.

$$^{subject}T_{plan3D} = f_2\left({}^{subject}T_{plane1}, {}^{subject}T_{plane2}, {}^{subject}T_{plane3}\right) \quad (3)$$

$$^{laser}T_{plan} = T_{laser}^{-1}\,T_{subject}\,{}^{subject}T_{plan3D} \quad (4)$$

C-arm calibration

Although the Siemens Arcadis Orbic C-arm is iso-centric and has 3D cone-beam reconstruction capabilities, we operated it under the Digital Radiography mode to better resemble an ordinary fluoroscopic X-ray. This system is serviced periodically and has a built-in geometric distortion correction function; consequently, additional distortion correction calibrations were not implemented. Accordingly, we assumed the C-arm to be a pinhole camera without distortion. A double-ring C-arm calibration phantom similar to that described by Livyatan et al. [22] but with 137 embedded fiducial steel ball bearings was used. We applied a cluster detection

algorithm, similar to that proposed by Cho et al. [23], to extract 2D positions of the ball bearings from X-ray images for calibration. Finally, we calculated C-arm intrinsic and extrinsic parameters by relating image pixels to 3D real-world points via equations previously proposed by Yakimovsky et al. [24] and Tate et al. [25]. The intrinsic (focal lengths and image-center point) and extrinsic (3D location of the image device pinhole) parameters are used for surgical planning.

Accuracy evaluation

Guidance accuracy was validated by tracking the position of a linear wire (length, 150 mm; diameter, 3 mm), which represented the desired surgical tool insertion path and the surgical tool itself. An infrared marker was attached for position tracking. Proper tool orientation alignment was indicated by parallel laser beams on side of the linear wire (Fig. 3) [15]. A guidance sleeve was also attached onto the linear wire to enlarge the wire's radius to better view projected laser lines.

We created a virtual coordinate system on a flat surface with its z-axis normal to the surface. We used a three factorial Box–Behnken (BB) experimental design method [26] to create 15 validation trials with different ground truth insertion path. These paths were each represented by a 4-by-4 transformation matrix. BB design factors and levels were as follows: xy-direction (−50/50, 0, 50/50 mm), polar angle (−30, 0, 30°), and azimuthal angle (−30, 0, 30°). Surgical planning was conducted using two 2D images taken at 90° angles for planning and three 2D images taken with 45° angle differences.

For each validation trial, the following procedure was performed. First, the ground truth insertion path was shown by the dual lasers in 3D space. The infrared attached linear wire was placed according to the lasers. Using this initial linear wire position, 2D images were taken for planning. The linear wire was removed while planning was performed. Once the 3D insertion path was generated, the laser was turned on. The linear wire was repositioned using guidance by laser. Final linear wire position was recorded once parallel laser beams were observed on the guidance sleeve. Proper alignment of linear wire with the laser beams required matching of five positional coordinates: the xyz translational coordinates, the polar angle (θ), and the azimuthal angle (ψ). The translational coordinates measured the laser's accurate Cartesian positioning of the insertion point. The two angles were used to determine alignment of the surgical tool during insertion, also referred to as insertion orientation.

Pin insertion using phantoms

The feasibility of the proposed system was tested by mimicking percutaneous guidewire insertion procedures common in fracture repair surgeries (Fig. 3). In this experiment, we inserted a total of 6 guidewire into 3 phantoms (Fig. 4) using commercially available orthopedic surgical tools from MicroAire. Bone structure and soft tissue were made of paint thinner coated plastic femur bone phantoms (SAWBONEs; SAWBONE Inc., USA) and polyvinyl chloride (Ludlow Composites, USA) of 30 mm thickness, respectively (Fig. 4). Realistically, bone and skin are not rigidly attached; thus, polyvinyl chloride was used to distort the actual location of the bone (Fig. 5). The patient coordinate system, CS_S, was created using an infrared marker attached to the sawbone.

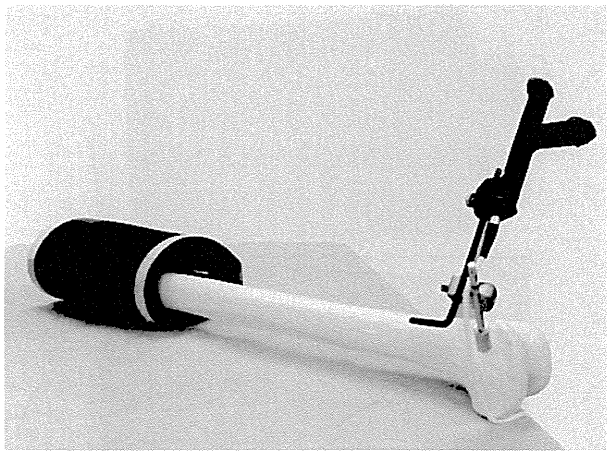

Fig. 4 A phantom of the human right femoral bone and soft tissue. Pedicle screw insertion experiments were performed on 3 phantoms. The material used to mimic soft tissue can be freely relocated depending on the desired location of insertion

Three X-ray images of the phantom were taken with angle difference of 45°. Insertions were separated into two categories: with anatomical landmark or with artificial landmark. In the former case, intramedullary nail insertion through the femoral head was performed. The shape of the femoral head acted as the anatomical landmark, and insertion plans were made through the center of the femoral head. In cases lacking anatomical landmarks, such as in bone reduction surgeries where insertions are made perpendicular to the bone shaft, artificial landmarks are provided. In our experiments requiring landmarks, a surgically used Kirschner (K) wire (MicroAire, Charlottesville, USA) placed perpendicular to the femur shaft of the phantom acted as the artificial landmark. The K-wire is linearly shaped, similar to the linear wire used for accuracy evaluation. We performed surgical planning referencing this K-wire. Upon completion, lasers were turned on and a guidewire was inserted. Each inserted guidewire was measured by locating its tip, the contact point with the phantom surface, and its end with an optically tracked stylus. Specifically, tip was calculated using three points on the guidewire circumference. Position and orientation errors were then given as the difference between each planned insertion and the final guidewire position in physical space.

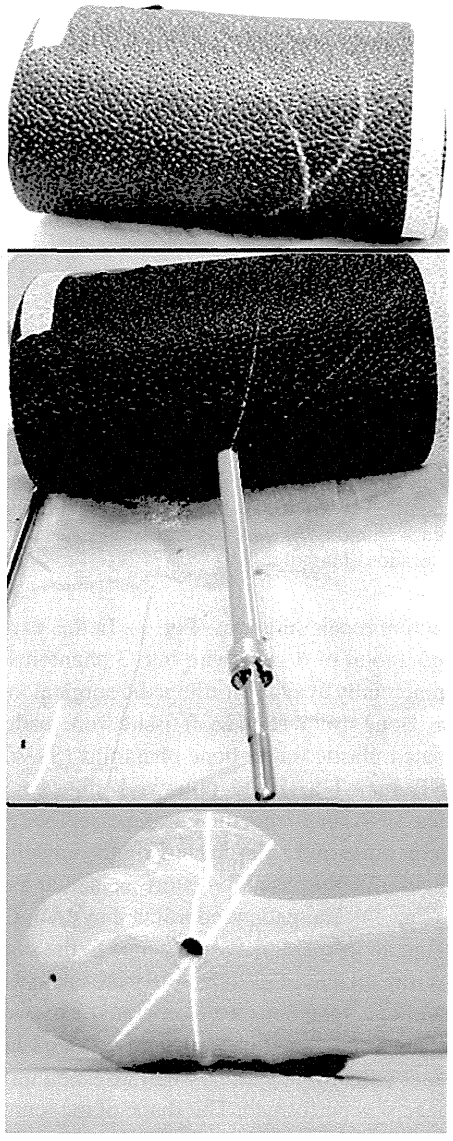

Fig. 5 *Top* laser being projected onto the phantom (femoral head cannot be visualized). *Middle* guidewire completely inserted into the phantom; proper orientation is indicated by parallel lasers. *Bottom* lasers being projected onto the bone after the removal of the soft tissue material and inserted guidewire

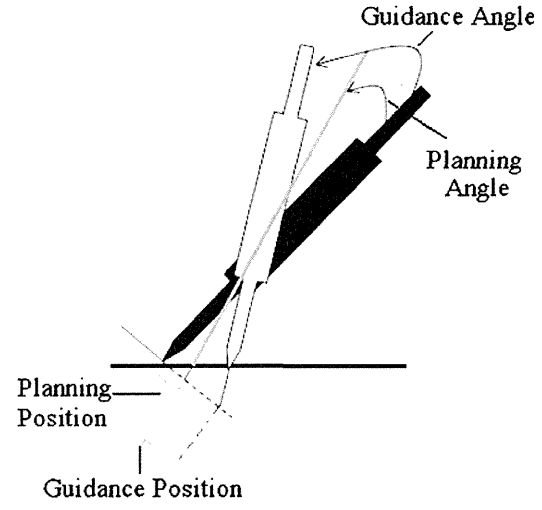

Fig. 6 The *black* needle represents the initial linear wire position; the *white* needle is the final linear wire position; and the *green* line is the planned insertion path in 3D space. Guidance error looks at the angular and positional differences between the initial and final needle positions. Planning error looks at the angular and positional differences between the initial needle position and planned insertion line

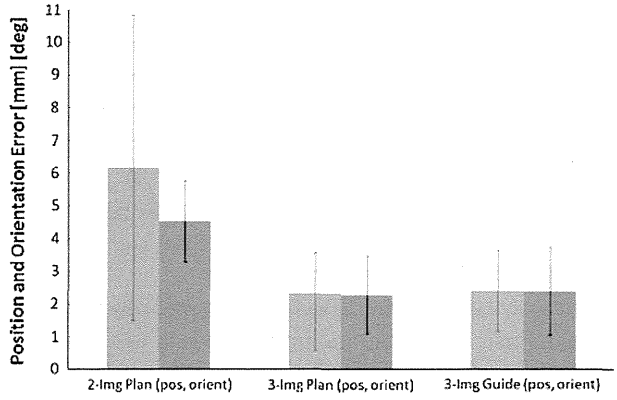

Fig. 7 Position and orientation errors shown in *blue* and *red*, respectively. Results include accuracies for 2-image planning, 3-image planning, and 3-image guidance

Results

Navigation accuracy

Fluorolaser accuracy validation looked at the displacement of relative tip locations between planed 3D insertion path, initial linear wire position, and final linear wire position. Since the binary lasers cannot indicate insertion depth, we report only the system's lateral errors. In particular, we calculated the difference in tip positions in a plane that is perpendicular and intersects the initial linear wire tip (Fig. 6). Planning accuracy refers to the error between actual insertion path and user-determined insertion path. A transformation matrix describing the user-generated 3D insertion path was obtained with its origin at the insertion point. Guidance accuracy refers to the error of the overall system. The two ends of the linear wire were registered to the attached AdapTrax marker. Thus, initial and final linear wire tip positions and orientation vectors in the world coordinate were obtained using simple transformation.

The results of the 15 validation trials are presented in Fig. 7. Planning accuracy of the system using two 2D images for planning was found to be 6.17 ± 4.68 mm, $4.53 \pm 1.24°$. Accuracy using linear regression of three 2D images for planning was found to be 2.32 ± 1.74 mm, $2.28 \pm 1.19°$. There

Table 1 Experimental results using physical space evaluation

	Femoral shaft insertion		Femoral head insertion	
Mean	2.05 (mm)	1.91°	2.12 (mm)	2.26°
SD	0.09 (mm)	0.70°	0.31 (mm)	2.26°
RMS	1.71 (mm)	1.73°	2.13 (mm)	2.26°

is a significant improvement in both position and orientation accuracy with the use of three images (P value: 1.06×10^{-2} and 1.21×10^{-4} for position and orientation, respectively).

Using three images, the RMS error of position and orientation accuracies was 2.86 mm and 2.55°, respectively. The overall guidance RMS error with the use of three 2D images was found to be 2.67 mm and 2.72° (2.40 ± 1.23 mm, 2.39 ± 1.34°). Moreover, Box–Behnken surface response analysis showed that no single factor in the 15 different three-factor three-level combinations (xy: − 50/50, 0, 50/50 mm; polar: −30, 0, 30°; azimuthal: −30, 0, 30°) contributed significantly more to the planning and guidance errors.

Phantom feasibility

We performed percutaneous guidewire insertion experiments using 3 sawbone phantoms for a total of 6 insertions: 3 perpendicular to the femur shaft and 3 through the femoral head. We performed feasibility analysis visually as well as by comparing the planning matrix and the final inserted guidewire position. A summary of the lateral errors is shown in Table 1. We obtained an RMS error of 1.71 mm and 1.73° for femoral shaft insertions using artificial landmark. Femoral head insertion using anatomical landmark (Fig. 8) yielded RMS error of 2.13 mm and 2.26°. Differences between femoral head and shaft insertions were not significant. Max error between all 6 insertions was 2.35 mm, 2.63°.

Visually, we observed parallel laser lines on the referenced K-wire in trials where artificial landmarks were used. The average overall operation time from image acquisition to insertion completion per insertion was less than 10 min. Average time for planning was 1 min and 8 s, where planning using anatomical landmarks took on average 1 min and 25 s and trials with artificial landmarks took 51 s. Drilling and insertion of the guidewire was the most time-consuming step in the entire operation.

Discussion

The Gertzbein and Robbins pedicular screw placement classification [27] is commonly used to evaluate accuracies of spine surgeries [28,29]. Using these standards, we conclude that navigational systems design for orthopedic percutaneous surgeries using 2D images can be considered precise and accurate when position and orientation errors are within 2 mm and 2°. Greater errors are allowed for long bone fracture reduction [30].

Using the fluorolaser navigation system, surgical outcomes can be affected by navigation accuracy and execution accuracy. The latter includes accuracies related to laser beam projection and surgical tool placement by the surgeon, both of which have been validated previously [15,20,21]. In this study, we evaluated the planning (navigation) error and overall guidance error of the system using a Box–Behnken surface response experimental design. We evaluated the lateral positioning error by computing the 2D difference of tip positions in a plane that is perpendicular to and intersects the insertion plan. Ideally, this tip represents the target point such as the femoral bone or spine. Our results indicate

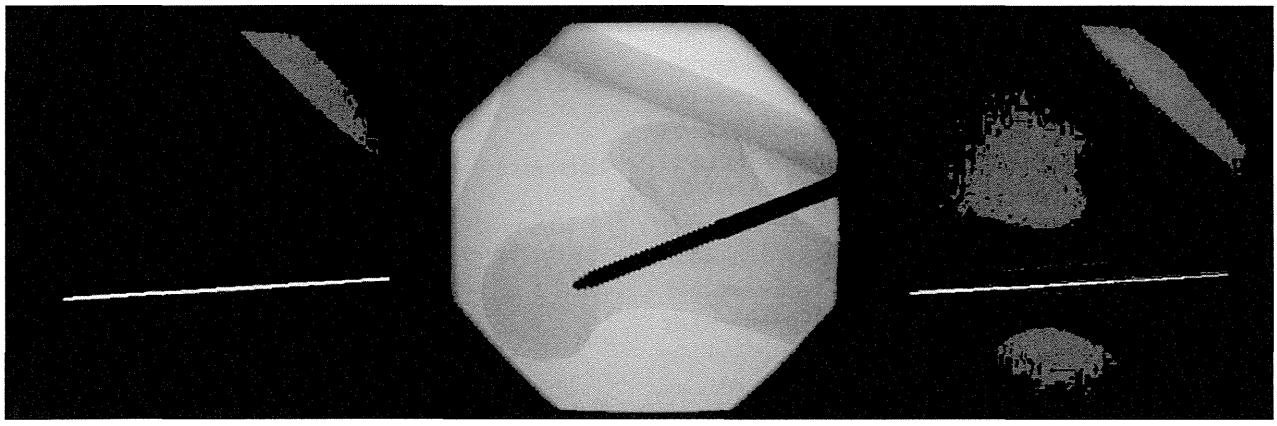

Fig. 8 X-ray images of a phantom containing the femoral head and soft tissue. *Left* X-ray image with insertion plan line shown in green. *Center* X-ray image of the phantom after pin insertion. *Right* overlay of insertion plan onto the center image

that while the accuracies are acceptable, the current system is not yet robust enough for clinical usage due to the high standard deviation. Furthermore, planning accuracy is limited by the C-arm fluoroscope calibration technique as well as user-based insertion path planning procedure. In the current calibration protocol, 100 fiducial marker positions in 2D and 3D were obtained via image processing and calculations, respectively. Compared with the laser guidance system using CT-based navigation, which had a phantom guidewire insertion RMS error of 1.39 mm, 1.03° [15], future calibration protocol should consider the increase in fiducial count or the use of multiple phantom images taken from different positions to improve system accuracy. Also, the current study took X-ray C-arm images only in one C-arm rotational plane. Future studies should consider the effects of relative C-arm positions toward accuracy.

The current planning procedure requires the aid of structural landmarks present on the X-ray image. This is the key to simplifying the interpretation of 3D positions from 2D images. However, anatomical landmarks may not always be available for all types of surgeries. Although no significant differences are detected between insertions made with and without anatomical landmarks, additions should be made onto the current system to ensure a simple and efficacious planning procedure. We intend to introduce artificial landmarks in the form of radiopaque stickers to be attached onto the patient skin. Nevertheless, the planning interface can be modified accordingly depending on the specific surgical task required.

We performed phantom experiments to validate the capabilities of percutaneous pin insertion procedures. Intraoperatively guidance was intuitive and insertion procedures were not interfered by the surrounding environment. Although fracture reduction surgery was one of the targeted surgical procedures of the original laser guidance system, we were unable to perform reduction experiments using the improved fluorolaser system. This was because relative insertion positions are essential in fixation-based reduction [31]. Future works should investigate other methods, such as visual servoing [32], to apply this new system into reduction surgeries. Furthermore, this study focused on orthopedic percutaneous surgeries; however, use of the dyna-CT function in X-ray C-arms may allow the proposed system to be useful in surgeries involving linear insertions into soft tissues.

Another future requirement is the introduction of insertion depth guidance. Depth guidance may be achieved using additional X-rays or attaching positioning trackers onto the tool. The former method would increase radiation exposure, while the latter introduces specialized surgical tools that limit the range of motion of surgeons during interventions. Another approach is to introduce additional mechanisms such as a physical stopper, a physical depth guide, or a depth guidance ring onto the surgical tool and surgical drill. Some surgical procedures currently use these types of tools. Also, a third laser source may also be a viable method that can guide depth without additional visualization mechanisms. Without additional mechanisms, this fluorolaser navigation system can only be used for surgical procedures that use surgical drills with depth guidance rings on their shaft. Nevertheless, addition of depth guidance may widely expand the applicable areas of our method.

Moving away from the conventional surgical navigation systems, we have presented the fluorolaser system, which allows navigated surgeries to be performed simply by aligning surgical tools at the crosshair of two laser beams. Surgical planning is performed using three X-ray images as opposed to complete CT. The system does not require surgeons to obtain navigation information from a secondary display source. This system does not require specialized or tracked surgical tools; it can thus be easily integrated into many surgical environments. Although this system is an improvement to conventional systems, future improvements and clinical assessments are necessary to fully validate its robustness in actual surgeries.

Conclusion

In conclusion, we have proposed the fluorolaser navigation system, which combines the fluoroscope-based navigation and laser guidance techniques to enable intuitive positioning of linear surgical tools to be inserted in percutaneous surgeries without preoperative CT/MRI volumes. Specifically, in vitro needle insertion path planning and phantom pedicle screw insertion experiments were performed using three 2D X-ray images from a C-arm and two laser beams for insertion guidance. Since the binary lasers cannot indicate insertion depth, we report only the system's lateral errors. Experimental results demonstrate that the fluorolaser navigation system has great potentials to ensure accurate and intuitive surgical tool insertion procedures without preoperative CT/MRI volumes and registration processes.

Conflict of interest None.

References

1. Schlenzka D, Laine T, Lund T (2000) Computer-assisted spine surgery. Eur Spine J 9(7):57–64. doi:10.1007/PL00010023
2. Fuchs H, State A, Pisano E, Garrett W, Hirota G, Livingston M, Whitton M, Pizer S (1996) Towards performing ultrasound-guided needle biopsies from within a head-mounted display visualization in biomedical computing. In: Höhne K, Kikinis R (eds), vol 1131. Lecture notes in computer science. Springer, Berlin, Heidelberg, pp 591–600. doi:10.1007/BFb0047002
3. Blackwell M, Nikou C, DiGioia AM, Kanade T (2000) An image overlay system for medical data visualization. Med Image Anal 4(1): 67–72. doi:10.1016/s1361-8415(00)00007-4

4. Fichtinger G, Deguet A, Masamune K, Balogh E, Fischer GS, Mathieu H, Taylor RH, Zinreich SJ, Fayad LM (2005) Image overlay guidance for needle insertion in CT scanner. IEEE Trans Biomed Eng 52(8):1415–1424
5. Liao H, Ishihara H, Tran H, Masamune K, Sakuma I, Dohi T (2008) Fusion of laser guidance and 3-D autostereoscopic image overlay for precision-guided surgery medical imaging and augmented reality. In: Dohi T, Sakuma I, Liao H (eds), vol 5128. Lecture notes in computer science. Springer, Berlin, Heidelberg, pp 367–376. doi:10.1007/978-3-540-79982-5_40
6. Volonté F, Pugin F, Bucher P, Sugimoto M, Ratib O, Morel P (2011) Augmented reality and image overlay navigation with OsiriX in laparoscopic and robotic surgery: not only a matter of fashion. J Hepato-Biliary-Pancreatic Sci 18(4): 506–509. doi:10.1007/s00534-011-0385-6
7. Gavaghan K, Oliveira-Santos T, Peterhans M, Reyes M, Kim H, Anderegg S, Weber S (2011) Evaluation of a portable image overlay projector for the visualisation of surgical navigation data: phantom studies. Int J Comput Assist Radiol Surg. doi:10.1007/s11548-011-0660-7
8. Malik JM, Kamiryo T, Goble J, Kassell NF (1995) Stereotactic laser-guided approach to distal middle cerebral artery aneurysms. Acta Neurochirurgica 132(1):138–144. doi:10.1007/bf01404862
9. Lavallee S, Toroccaz J, Sautot P et al (1996) Computer-assisted spinal surgery using anatomy-based registration. In: Computer-Integrated Surgery: Technology and Clinical Applications, the MIT Press, pp 425–229
10. Hussman KL, Chalouplca JC, Berger SB (1998) Frameless laser-guided stereotaxis: a system for CT-monitored neurosurgical interventions. Stereotect Funct Neurosurg 71:62–75. doi:10.1159/000029649
11. Glossop N, Wedlake C, Moore J, Peters T, Wang Z (2003) Laser projection augmented reality system for computer assisted surgery medical image computing and computer-assisted intervention—MICCAI 2003. In: Ellis R, Peters T (eds), vol 2879. Lecture Notes in Computer Science. Springer, Berlin, Heidelberg, pp 239–246. doi:10.1007/978-3-540-39903-2_30
12. Marmurek J, Wedlake C, Pardasani U et al (2005) Image-guided laser projection for port placement in minimally invasive surgery. In: Medicine meets virtual reality 14, vol 119. IOS Press, pp 367–372
13. Nitta N, Takahashi M, Tanaka T, Takazakura R, Sakashita Y, Furukawa A, Murata K, Shimoyama K (2007) Laser-guided computed tomography puncture system: simulation experiments using artificial phantom lesions and preliminary clinical experience. Radiat Med 25(4):187–193. doi:10.1007/s11604-006-0116-0
14. Sasama T, Sugano N, Sato Y, Momoi Y, Koyama T, Nakajima Y, Sakuma I, Fujie M, Yonenobu K, Ochi T, Tamura S (2002) A novel laser guidance system for alignment of linear surgical tools: its principles and performance evaluation as a man—machine system medical image computing and computer-assisted intervention—MICCAI 2002. In: Dohi T, Kikinis R (eds) vol 2489. Lecture notes in computer science. Springer, Berlin, Heidelberg, pp 125–132. doi:10.1007/3-540-45787-9_16
15. Nakajima Y, Sasama T, Momoi Y, Sugano N, Tamura Y, Dohi T, Lim S, Sakuma I, Mitsuishi M, Koyama T, Yonenobu K, Ohnishi I, Bessho M, Ohashi S, Nakamura K (2012) Surgical tool alignment guidance by drawing two cross-sectional laser-beam planes. IEEE Trans Biomed Eng (in-press)
16. Foley KT, Simon DA, Rampersaud YR (2001) Virtual fluoroscopy: computer-assisted fluoroscopic navigation. Spine 26(4):347–351
17. Hofstetter R, Slomczykowski M, Sati M, Nolte L-P (1999) Fluoroscopy as an imaging means for computer-assisted surgical navigation. Comput Aided Surg 4(2): 65–76. doi:10.3109/10929089909148161
18. Wiest P, Locken J, Heintz P, Mettler F (2002) CT scanning: a major source of radiation exposure. Semin Ultsd CT MRI 23(5):402–410. doi:10.1053/sult.2002.34010
19. Smith H, Welsch M, Sasso R, Vaccaro A (2008) Comparison of radiation exposure in lumbar pedicle screw placement with fluoroscopy vs computer-assisted image guidance with intraoperative three-dimensional imaging. J Spinal Cord Med 31(5):532–537
20. Nakajima Y, Yamamoto H, Sato Y, Sugano N, Momoi Y, Sasama T, Koyama T, Tamura Y, Yonenobu K, Sakuma I, Yoshikawa H, Ochi T, Tamura S (2004) Available range analysis of laser guidance system and its application to monolithic integration with optical tracker. Int Congr Ser 1268(0): 449–454. doi:10.1016/j.ics.2004.03.127
21. Lim S, Douke T, Onogi S et al (2010) Assessment for the feasibility of external-fixation pin guidance using laser navigation. Jpn Soc Comp Aid Surg 12:511–518
22. Livyatan H, Yaniv Z, Joskowicz L (2002) Robust automatic C-arm calibration for fluoroscopy-based navigation: a practical approach medical image computing and computer-assisted intervention—MICCAI 2002. In: Dohi T, Kikinis R (eds) vol 2489. Lecture notes in computer science. Springer, Berlin, Heidelberg, pp 60–68. doi:10.1007/3-540-45787-9_8
23. Cho PS, Johnson RH (1998) Automated detection of bb pixel clusters in digital fluoroscopy images. Phys Med Biol 42:2677–2682
24. Yakimovsky Y, Cunningham R (1978) A system for extracting three-dimensional measurements from a stereo pair of TV cameras. Comput Graph Image Process 7(2):195–210. doi:10.1016/0146-664x(78)90112-0
25. Tate P, Lachine V, Fu L, Croitoru H, Sati M (2001) Performance and robustness of automatic fluoroscopic image calibration in a new computer assisted surgery system medical image computing and computer-assisted intervention—MICCAI 2001. In: Niessen W, Viergever M (eds) vol 2208. Lecture notes in computer science. Springer, Berlin, Heidelberg, pp 1130–1136. doi:10.1007/3-540-45468-3_135
26. Ferreira S, Bruns R, Ferreira H, Matos G, David J, Brandao G, Silva E, Portugal L, Reis P, Souza A, Santos W (2007) Box-Behnken design: an alternative for the optimization of analytical methods. Analytica Chimica Acta 597(2):179–186. doi:10.1016/j.aca.2007.07.011
27. Gertzbein S, Robbins S (1990) Accuracy of pedicular screw placement in vivo. Spine 15(1):11–14
28. Pechlivanis I, Kiriyanthan G, Engelhardt M, Scholz M, Lucke S, Harders A, Schmieder K (2009) Percutaneous placement of pedicle screws in the lumbar spine using a bone mounted miniature robotic system. Spine 34(4):392–398
29. Belmont P, Klemme W, Dhawan A, Polly D (2001) In vivo accuracy of thoracic pedicle screws. Spine 26(21):2340–2346
30. Weil Y, Liebergall M, Mosheiff R, Helfet D, Pearle A (2007) Long bone fracture reduction using a fluoroscopy-based navigation system: a feasibility and accuracy study. Comp Aided Surg 12(5): 295–302
31. Navab N, Bascle B, Loser M, Geiger B, Taylor R (2000) Visual servoing for automatic and uncalibrated needle placement for percutaneous procedures. In: Proceedings of the IEEE Conference on Computer vision and pattern recognition, 2000, vol.322. pp 327–334
32. Croitoru H, Ellis RE, Prihar R, Small CF, Pichora DR (2001) Fixation-based surgery: a new technique for distal radius osteotomy. Comput Aided Surg 6(3):160–169. doi:10.1002/igs.1019

Cancer Chemother Pharmacol (2013) 71:511–521
DOI 10.1007/s00280-012-2041-5

ORIGINAL ARTICLE

Randomized trial of chemoradiotherapy and adjuvant chemotherapy with nimustine (ACNU) versus nimustine plus procarbazine for newly diagnosed anaplastic astrocytoma and glioblastoma (JCOG0305)

Soichiro Shibui · Yoshitaka Narita · Junki Mizusawa · Takaaki Beppu · Kuniaki Ogasawara · Yutaka Sawamura · Hiroyuki Kobayashi · Ryo Nishikawa · Kazuhiko Mishima · Yoshihiro Muragaki · Takashi Maruyama · Junichi Kuratsu · Hideo Nakamura · Masato Kochi · Yoshio Minamida · Toshiaki Yamaki · Toshihiro Kumabe · Teiji Tominaga · Takamasa Kayama · Kaori Sakurada · Motoo Nagane · Keiichi Kobayashi · Hirohiko Nakamura · Tamio Ito · Takahito Yazaki · Hikaru Sasaki · Katsuyuki Tanaka · Hideaki Takahashi · Akio Asai · Tomoki Todo · Toshihiko Wakabayashi · Jun Takahashi · Shingo Takano · Takamitsu Fujimaki · Minako Sumi · Yasuji Miyakita · Yoichi Nakazato · Akihiro Sato · Haruhiko Fukuda · Kazuhiro Nomura

Received: 6 October 2012 / Accepted: 22 November 2012 / Published online: 11 December 2012

Abstract
Purpose Glioblastoma (GBM) is one of the worst cancers in terms of prognosis. Standard therapy consists of resection with concomitant chemoradiotherapy. Resistance to nimustine hydrochloride (ACNU), an alkylating agent, has been linked to methylguanine DNA methyltransferase (MGMT). Daily administration of procarbazine (PCZ) has been reported to decrease MGMT activity. This study investigated the efficacy of ACNU + PCZ compared to ACNU alone for GBM and anaplastic astrocytoma (AA).

Methods Patients (20–69 years) who had newly diagnosed AA and GBM were randomly assigned to receive radiotherapy with ACNU alone or with ACNU + PCZ. The primary endpoint was overall survival (OS). This was designed as a phase II/III trial with a total sample size of 310 patients and was registered as UMIN-CTR C000000108.
Results After 111 patients from 19 centers in Japan were enrolled, this study was terminated early because temozolomide was newly approved in Japan. The median OS and median progression-free survival (PFS) with ACNU alone ($n = 55$) or ACNU + PCZ ($n = 56$) in the

S. Shibui (✉) · Y. Narita · Y. Miyakita · K. Nomura
Department of Neurosurgery and Neuro-Oncology,
National Cancer Center Hospital, 5-1-1,
Tsukiji, Chuo-ku, Tokyo 104-0045, Japan
e-mail: sshibui@ncc.go.jp

J. Mizusawa · A. Sato · H. Fukuda
Japan Clinical Oncology Group Data Center,
National Cancer Center, Tokyo, Japan

T. Beppu · K. Ogasawara
Department of Neurosurgery, Iwate Medical University,
Iwate, Japan

Y. Sawamura · H. Kobayashi
Department of Neurosurgery, Hokkaido University Graduate
School of Medicine, Hokkaido, Japan

R. Nishikawa · K. Mishima
Department of Neuro-Oncology/Neurosurgery,
International Medical Center, Saitama Medical University,
Saitama, Japan

Y. Muragaki · T. Maruyama
Department of Neurosurgery,
Tokyo Women's Medical University, Tokyo, Japan

J. Kuratsu · H. Nakamura · M. Kochi
Department of Neurosurgery,
Kumamoto University,
Kumamoto, Japan

Y. Minamida · T. Yamaki
Department of Neurosurgery,
Sapporo Medical University,
Sapporo, Japan

T. Kumabe · T. Tominaga
Department of Neurosurgery,
Tohoku University School of Medicine, Miyagi, Japan

T. Kayama · K. Sakurada
Department of Neurosurgery, Faculty of Medicine,
Yamagata University, Yamagata, Japan

intention-to-treat population were 27.4 and 22.4 months ($p = 0.75$), and 8.6 and 6.9 months, respectively. The median OS and median PFS of the GBM subgroup treated with ACNU alone ($n = 40$) or ACNU + PCZ ($n = 41$) were 19.0 and 19.5 months, and 6.2 and 6.3 months, respectively. Grade 3/4 hematologic adverse events occurred in more than 40 % of patients in both arms, and 27 % of patients discontinued treatment because of adverse events.

Conclusions The addition of PCZ to ACNU was not beneficial, in comparison with ACNU alone, for patients with newly diagnosed AA and GBM.

Keywords Glioblastoma · Anaplastic astrocytoma · Nimustine · ACNU · Procarbazine · MGMT

Abbreviations

GBM	Glioblastoma
AA	Anaplastic astrocytoma
ACNU	Nimustine hydrochloride
BCNU	Carmustine
TMZ	Temozolomide
MGMT	Methylguanine DNA methyltransferase
WHO	World Health Organization
PFS	Progression-free survival
OS	Overall survival
RT	Radiotherapy
HR	Hazard ratio
AE	Adverse event
ND	Not determined
CR	Complete response
PR	Partial response
SD	Stable disease
PD	Progressive disease
WBC	White blood cell
3D-CRT	Three-dimensional conformal radiotherapy
CT	Computed tomography
IMRT	Intensity-modulated radiation therapy
BEV	Beam's eye views
DVH	Dose–volume histograms
GTV	Gross tumor volume
CTV	Clinical target volume
PTV	Planning target volume
ICRU	International Commission on Radiation Units
FLAIR	Fluid-attenuated inversion recovery
OAR	Organ-at-risk

Introduction

Glioblastoma (GBM) is one of the worst cancers in terms of prognosis, with almost all patients experiencing progression without cure. According to the report of the Brain Tumor Registry of Japan, the %5-year survival of World Health Organization (WHO) grade IV GBM is 6.9 % and that of WHO grade III anaplastic astrocytoma (AA) is 33.9 % [1].

Standard therapy against GBM consists of the maximal resection that is safely possible, with concomitant chemo-radiotherapy. Currently, temozolomide (TMZ) is the

M. Nagane · K. Kobayashi
Department of Neurosurgery,
Kyorin University Faculty of Medicine, Tokyo, Japan

H. Nakamura · T. Ito
Department of Neurosurgery,
Nakamura Memorial Hospital, Hokkaido, Japan

T. Yazaki · H. Sasaki
Department of Neurosurgery,
Keio University School of Medicine, Tokyo, Japan

K. Tanaka
Department of Neurosurgery, St. Marianna University
School of Medicine, Kanagawa, Japan

H. Takahashi
Department of Neurosurgery, Brain Research Institute,
Niigata University, Niigata, Japan

A. Asai
Department of Neurosurgery,
Saitama Medical Center, Saitama, Japan

T. Todo
Department of Neurosurgery, University of Tokyo, Tokyo, Japan

T. Wakabayashi
Department of Neurosurgery, Nagoya University Graduate
School of Medicine, Nagoya, Japan

J. Takahashi
Department of Neurosurgery,
Kyoto University Graduate School of Medicine,
Kyoto, Japan

S. Takano
Department of Neurosurgery, Tsukuba University,
Tsukuba, Japan

T. Fujimaki
Department of Neurosurgery,
Teikyo University School
of Medicine, Tokyo, Japan

M. Sumi
Department of Radiation-Oncology,
National Cancer Center Hospital,
Tokyo, Japan

Y. Nakazato
Department of Pathology,
Gunma University, Gunma, Japan

standard agent used in the treatment of GBM. However, before the TMZ era, nitrosourea had been widely used for GBM and AA. The Glioma Meta-analysis Trialists Group described that chemotherapy including nitrosourea showed significant prolongation of survival, with a hazard ratio of 0.85 ($p < 0.0001$) [2].

Nimustine hydrochloride (ACNU) was developed in Japan, and for more than 20 years since 1980, it has been the standard chemotherapeutic agent against gliomas [3]. Wolff et al. [4] analyzed 364 studies, including a total of 24,193 patients with high-grade glioma, and reported that the survival gain in the 15 ACNU-treated cohorts was 8.9 months, compared to those who received different drugs or no chemotherapy. Takakura et al. [5] reported that the overall survival (OS) of AA and GBM treated by radiotherapy (RT) and concomitant ACNU were 36 and 12 months, respectively. Furthermore, the response rate of a more than 50 % reduction in tumor size was 46.2 % in both AA and GBM. Alkylating agents, including ACNU and procarbazine (PCZ), confer cytotoxic effects on glioma cells by alkylation at the O^6-position of guanine in DNA. This results in the formation of DNA cross-links [6]. Methylguanine DNA methyltransferase (MGMT) removes methylation damage induced by nitrosourea from the O^6-position of DNA guanines before cell injury, and this enzyme was detectable in 76 % of glioma tissues [7]. MGMT in glioma cells is a primary defense against nitrosourea, but the cellular methyltransferase activity of MGMT is exhausted after MGMT takes effect. Daily administration of PCZ for 10 days was reported to cause the accumulation of O^6-methylguanine; it also decreased MGMT activity in rat liver [8] and lymphocytes in lymphoma patients [9]. Inhibition of MGMT by O^6-benzylguanine increased the cytotoxicity of TMZ and carmustine (BCNU) to tumor cells [10]. From these results, it can be predicted that daily administration of PCZ, by depleting MGMT activity, will increase the efficacy of ACNU against AA and GBM.

To prove this hypothesis and establish a more potent standard therapy for AA and GBM, the Brain Tumor Study Group of the Japan Clinical Oncology Group (JCOG) conducted this clinical trial. The study was terminated at the end of the phase II part. The current report describes the final outcome of the study.

Subjects and methods

Patient eligibility criteria

Patients aged 20 to less than 70 years of age who had newly diagnosed and histologically proven supratentorial GBM or AA were eligible for this study. Patients were enrolled between 3 and 14 days after their operation. To be eligible, a patient's preoperative MRI had to show that more than 50 % of the tumor was located in supratentorial areas, except the optic nerve, olfactory nerve, or pituitary gland. Eligible patients had Eastern Cooperative Oncology Group (ECOG) performance status (PS) of 0–2 or 3 (only in cases with neurologic symptoms caused by a tumor) and adequate hematologic, pulmonary, renal, and hepatic function, defined as follows: white blood cell (WBC) count $\geq 3.0 \times 10^3$/mL, hemoglobin level ≥ 8.0 g/dL, platelets count $\geq 1.0 \times 10^6$/mL, aspartate transaminase (AST) level ≤ 100 IU/L, alanine transaminase (ALT) level ≤ 100 IU/L, serum creatinine level ≤ 1.0 mg/dL. Additionally, written informed consent was obtained from all the participating patients. We excluded patients with multiple or disseminated tumors or large tumors in which the planned target volume for irradiation exceeded 1/3 of the whole-brain volume. Additionally, we also classified as ineligible any patient who was pregnant, had meningitis, pneumonia, diabetes mellitus with insulin injection, myocardial infarction, or unstable angina pectoris within the last 3 months, mental disorders, a history of pulmonary fibrosis or interstitial pneumonia, or other forms of active cancer occurring within 5 years of treatment. The study protocol was approved by JCOG Protocol Review Committee and institutional review board at each center.

Treatment

After the confirmation of the eligibility criteria, registration was made by telephone or fax to the JCOG Data Center. Patients were randomized within 14 days of surgery to either ACNU with RT (the control arm, A) or to ACNU + PCZ with RT (the experimental arm, B) (Fig. 1a) by a minimization method with adjustment factors consisting of histology (GBM vs. AA), age (younger than 60 vs. 60 years or older), residual tumor (presence vs. absence), and institution. Residual tumor was assessed using a gadolinium-enhanced MRI obtained within 72 h of the surgery.

Radiotherapy with concomitant chemotherapy was started within 3 weeks after the surgery. Patient positioning and immobilization with an individual head mask and computed tomography (CT)-based planning were required. Treatment was delivered using linear accelerators with nominal energies ≥ 4 MV. Intensity-modulated radiation therapy (IMRT) technique was not permitted. All fields were to be treated every day. Three-dimensional conformal radiotherapy (3D-CRT) planning including the use of beam's eye views (BEV) and dose–volume histograms (DVH) were recommended for volumetric dose evaluation. Quality assurance reviews were done at the Radiotherapy Support Centre in Tokyo, Japan, with feedback sent to each

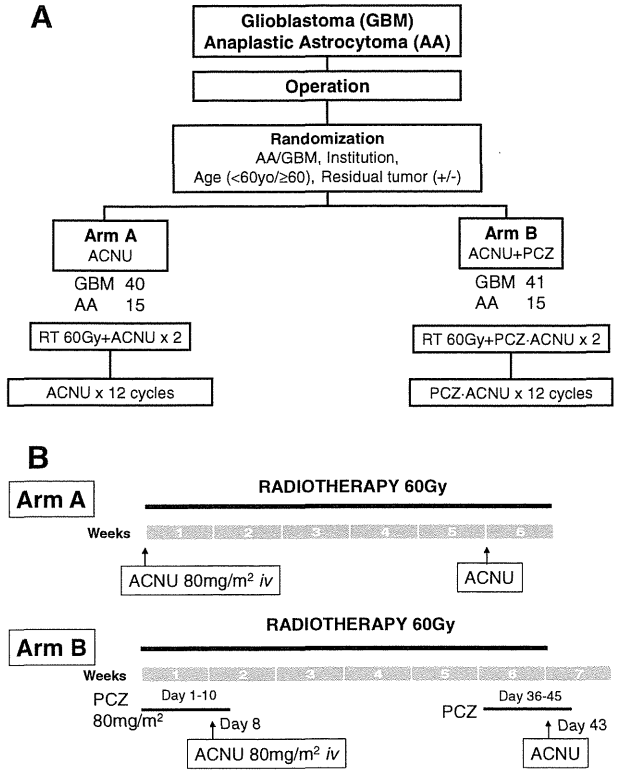

Fig. 1 **a** Study design of JCOG 0305: RT + ACNU versus RT + ACNU + PCZ; 40 patients with GBM and 15 patients with AA were assigned to *arm A*, and 41 patients with GBM and 15 patients with AA were assigned to *arm B*. **b** Treatment schedule of RT + ACNU (*Arm A*) and RT + ACNU + PCZ (*Arm B*)

institution by the radiotherapy study coordinator (Minako Sumi). The minimum and maximum dose to the PTV should be comprised between 95 and 107 % of the International Commission on Radiation Units (ICRU) reference point dose. The gross tumor volume (GTV) was defined as the primary tumor with or without enhancement on CT or magnetic resonance imaging (MRI). The clinical target volume 1(CTV1) included GTV, the resection cavity and surrounding edema (high-intensity area on T2-weighted or fluid-attenuated inversion recovery (FLAIR) image) plus a 1.5-cm margin. The CTV2 included GTV and the resection cavity plus a 1.5-cm margin. Planning target volume (PTV) was defined as CTV plus a margin of 0.5 cm or more. The doses for PTV1 and PTV2 were 50 and 10 Gy, respectively. The protocol required contouring organ-at-risk (OAR), including optic chiasm, brain stem, and retina. Cumulative doses to the optic chiasm and brainstem were limited to a maximum dose of 50 and 45 Gy for the retina.

In the control arm A, 80 mg/m^2 of ACNU was administered intravenously on days 1 and 36 during RT (Fig. 1b). In the experimental arm B, 80 mg/m^2 of oral PCZ was administered daily from days 1 to 10 and days 36 to 45, and given together with intravenous ACNU (80 mg/m^2) on days 8 and 43. Adjuvant therapy consisting of 80 mg/m^2 of ACNU alone in arm A or ACNU plus PCZ (PCZ: 80 mg/m^2 orally on days 1–10, ACNU: 80 mg/m^2 intravenously on day 8) in arm B started 56 days from the final administration of ACNU and was given every 8 weeks, for up to 12 cycles. Doses of ACNU and PCZ were calculated using actual body surface area, reduced for toxicity, and were not escalated.

Evaluations and follow-up

Baseline and follow-up examinations included vital signs, subjective symptoms, neurologic examination, MRI scan, and blood and serum laboratory examinations. For each patient, these examinations were performed weekly, with the exception of MRI scans, which were performed between the end of the initial chemoradiotherapy and the beginning of adjuvant therapy. All examinations were performed before each cycle of adjuvant chemotherapy, at a frequency of nearly every 2 months. After completion of the treatment protocol, patients were assessed every 3 months until progression. Toxicity was graded using the National Cancer Institute Common Toxicity Criteria (version 2). Findings of radiation necrosis were also assessed on MRI. Each patient was required to undergo a follow-up examination for at least 2 years from the date of randomization.

Tumor progression on MRI was defined according to Response Evaluation Criteria in Solid Tumors (RECIST), version 1.0 [11]. Progression of disease was defined as a 20 % increase in tumor size, as shown by contrast-enhanced imaging, or the development of new lesions, neurologic deterioration, or death by any cause. Further treatment at recurrence or progression was discretionary, but recorded.

A central pathology review by 3 independent pathologists (Yoichi Nakazato, a member of the Working Group for WHO 2007 classification; Nobuaki Funata; and Toru Iwaki) was performed and determinations given. A central review of radiological response was also performed.

Statistical analysis

When we planned this study, TMZ had been widely approved and was used worldwide. However, TMZ was not available in Japan. ACNU remained the standard therapy in Japan, but there was no sufficient data regarding this treatment. We planned a phase II/III clinical trial, with the phase II part designed to confirm the feasibility of ACNU and ACNU + PCZ.

The primary and secondary endpoints for the phase II part were %6-month survival and adverse events (AEs) in ACNU + PCZ arm. The primary endpoint of the phase III part was OS, while the secondary endpoints were PFS, response rate, complete response rate, and AEs.

Overall survival was calculated from the date of random assignment to the date of death from any cause and censored at the last follow-up for event-free patients. PFS was calculated from the date of randomization to the date of progression or death from any cause and censored at the last verifiable progression-free date for event-free patients. OS and PFS were estimated by the Kaplan–Meier method. OS was analyzed by the stratified log-rank test for eligible patients with adjustment factors, excluding institution. Unstratified log-rank tests were used for the analysis of PFS and subgroup analyses of OS and PFS. Fisher's exact test was used for categorical data. All p values are two-sided, except for primary analysis of OS.

We assumed %2-year survivals in AA and GBM for arm A were 50 and 20 %, and the ratio of those patients with AA or GBM enrolled in this study was expected to be 2:3. The phase III study was designed to enroll 155 patients per arm with 5 years of accrual and 2 years of follow-up, including those for the phase II part and about 10 % of ineligible patients, to achieve at least 75 % power to detect a hazard ratio (HR) of 0.74, with a one-sided alpha of 0.05 [12].

Three interim analyses were planned. The first was planned during phase II to test whether %6-month survival in arm A was superior to the predefined threshold (80 %), with a one-sided alpha of 0.1 and beta of 0.2, when 56 patients were included in ACNU + PCZ arm. The second and third interim analyses of OS were planned during phase III. For analyses of phase III part, multiplicity was adjusted by the Lan and DeMets alpha-spending function with the O'Brien and Fleming stopping boundary to control the type I error for primary endpoint.

In March 2007, protocol was amended to stop patient accrual after 111 patients had enrolled and to carry out the final analysis without planned interim analyses for both of phase II and phase III part. This was done because toxicity of both arms was unexpectedly high in phase II and because TMZ became available in Japan.

All statistical analyses were performed using SAS software, release 9.1 (SAS Institute, Cary, NC).

This trial is registered with UMIN-CTR (www.umin.ac.jp/ctr/), number C000000108.

Results

Patient characteristics

A total of 111 patients from 19 centers were randomly assigned to arm A ($n = 55$) or arm B ($n = 56$) from March 2004 to September 2006. Primary analyses were performed in September 2007, and the updated analyses were completed in July 2009. All patients were eligible for this study. Baseline characteristics were well balanced between the arms (Table 1). The median ages for arms A and B were 56 and 54 years, respectively. Total numbers for AA and GBM patients were 15 (27.3 %) and 40 (72.7 %) in arm A and 15 (26.8 %) and 41 (73.2 %) in arm B. PS 0 to 1 in arms A and B were 45 (81.8 %) and 41 (73.2 %), respectively. Eighteen (32.7 %) patients in arm A and 21 (37.5 %) patients in arm B underwent gross total removal, and no residual tumor was confirmed on MRI scans. The median duration of follow-up was 20.2 (range 0–48.0 months) for all eligible patients.

Treatment

Patient compliance with the treatment regimen is depicted in Table 2. Among the 111 total patients, 1 patient in arm A died from pulmonary embolism before the beginning of initial chemoradiotherapy. Fifty-three (96.3 %) patients in arm A completed initial chemoradiotherapy and received ACNU twice. In arm B, 48 out of 56 (85.7 %) patients received 2 cycles of PCZ + ACNU, and 8 patients (14.3 %) received 1 cycle of PCZ + ACNU in initial chemoradiotherapy. Eighteen (32.7 %) patients in arm A and 20 (35.7 %) patients in arm B failed to start adjuvant chemotherapy. Furthermore, 14 (25.5 %) patients in arm A and 23 (41.1 %) patients in arm B discontinued protocol therapy by the fourth cycle of adjuvant chemotherapy. The numbers of patients who received 4 cycles of chemotherapy or more were 23 (41.8 %) and 13 (23.2 %) in arm A and B, respectively. Only 5 (9.1 %) patients in arm A and 2 (3.6 %) patients in arm B completed the full protocol therapy. Nineteen (34.5 %) patients in arm A and 22 (39.3 %) patients in arm B discontinued the protocol for reasons other than completion of protocol or disease progression [arm A: 31 (56.4 %), arm B: 32 (57.1 %)]. Reasons for discontinuation were as follows: AEs [arm A: 6 (10.9 %), arm B: 13 (23.2 %)]; patient refusal related to AE

Table 1 Baseline characteristics in the ITT population

	Arm A ($n = 55$) (RT + ACNU)	Arm B ($n = 56$) (RT + PCZ + ACNU)
Age	56 (24–69)	54 (24–69)
Sex		
Male	32 (58.2 %)	33 (58.9 %)
Female	23 (41.8 %)	23 (41.1 %)
PS		
0, 1	45 (81.8 %)	41 (73.2 %)
2, 3	10 (18.2 %)	15 (26.8 %)
Histology		
Grade 3 (AA)	15 (27.3 %)	15 (26.8 %)
Grade 4 (GBM)	40 (72.7 %)	41 (73.2 %)
Surgery		
Gross total removal	18 (32.7 %)	21 (37.5 %)
Partial removal	30 (54.5 %)	26 (46.4 %)
Biopsy only	7 (12.7′ %)	9 (16.1 %)

Table 2 Compliance

	Arm A ($n = 55$) (RT + ACNU)	Arm B ($n = 56$) (RT + PCZ + ACNU)
RT (completion)	54 (98.2 %)	56 (100 %)
Initial chemotherapy		
1 cycle	1 (1.8 %)	8 (14.3 %)
2 cycles	53 (96.4 %)	48 (85.7 %)
Adjuvant chemotherapy		
None	18 (32.7 %)	20 (35.7 %)
1–3 cycles	14 (25.5 %)	23 (41.1 %)
4–6 cycles	9 (16.4 %)	7 (12.5 %)
7–11 cycles	9 (16.4 %)	4 (7.1 %)
12 cycles (completion)	5 (9.1 %)	2 (3.6 %)

[arm A: 3 (5.5 %), arm B: 8 (14.3 %)]; and patient refusal not related to AE [arm A: 7 (12.7 %), arm B: 1 (1.8 %)].

After discontinuation of the protocol, 28 (50.9 %) patients in arm A and 29 (51.8 %) patients in arm B received TMZ as further treatment.

Central review of histology

The central pathology review diagnosis of all cases was performed according to the WHO 2007 classification (Table 3). Among 81 GBM in the intention-to-treat (ITT) population, 69 (85.2 %), 4 (4.9 %), 3 (3.7 %), 2 (2.5 %), and 3 (3.7 %) were diagnosed as GBM, anaplastic oligoastrocytoma (AOA), anaplastic oligodendroglioma (AO), AA, and others, respectively. Only 10 cases (33.3 %) were diagnosed as AA among the 30 AA in the ITT population, while 8 (26.7 %), 5 (16.7 %), 3 (10.0 %), 2 (6.7 %), and 2 (6.7 %) were confirmed as GBM, AOA, diffuse astrocytoma, pilocytic astrocytoma, and others, respectively. Among all 111 cases, phenotype change of astrocytic to oligodendroglial tumor occurred in 14 cases (12.6 %). Finally, 77 and 12 patients were diagnosed with GBM and AA, respectively, by central pathology review.

Response rate

The overall radiographic response rate for 66 measurable diseases after surgery, based on RECIST guideline, was assessed by Diagnostic Radiology Committee. The response rate was 21.2 % (7/33) in arm A and 6.1 % (2/33) in arm B. In GBM patients from the ITT population, response rates were 25.0 % in arm A [3 CR (complete response), 2 PR (partial response), 1 SD (stable disease), 14 PD (progressive disease)] and 9.1 % in arm B [1 CR, 1 PR, 1 SD, 19 PD] ($p = 0.23$). In AA patients from the ITT population, response rates were 15.4 % in arm A (2 PR, 1 SD, 10 PD) and 0 % in arm B (11 PD) ($p = 0.48$).

Progression-free survival

In the entire ITT population, PFS was 8.6 months [95 % confidence interval (CI); 5.1–20.5] in arm A ($n = 55$, 44 events), compared with 6.9 months (95 % CI 5.1–9.0, $p = 0.36$) in arm B ($n = 56$, 47 events) (Fig. 2a). According to grades in the ITT population, PFS of GBM in arm A ($n = 40$, 33 events) and B ($n = 41$, 35 events) was 6.2 (95 % CI 4.2–13.2) and 6.3 months (95 % CI 3.0–8.9), respectively ($p = 0.35$) (Fig. 2b). PFS of AA in arm A ($n = 15$, 11 PD) and B ($n = 15$, 12 events) was 8.6 (95 % CI 5.1–35.4) and 9.0 months (95 % CI 5.8–21.8), respectively ($p = 0.83$) (Fig. 2c). No difference was observed between the arms in any subgroup defined by histology, presence of remaining tumor, or age under or over 60.

In the subgroup defined by central pathology review, the PFS of GBM in arms A ($n = 37$, 33 events) and B ($n = 40$, 36 events) was 5.1 (95 % CI 4.2–10.3) and 5.7 months (95 % CI 2.7–8.4), respectively ($p = 0.49$) (Fig. 2d). The PFS of AA and AOA in arm A ($n = 9$, 4 events) and B ($n = 12$, 9 events) was ND (not determined) and 7.9 months (95 % CI 5.2–22.5), respectively ($p = 0.21$).

Table 3 Local diagnosis and central pathology review

Grade	Histology	Local diagnosis	Central pathology review		
			Total	Arm A	Arm B
IV	*Glioblastoma*	83	77	37	40
III	*Anaplastic astrocytoma*	30	12	6	6
III	Anaplastic oligoastrocytoma		9	3	6
III	Anaplastic oligodendroglioma		3	2	1
III	Anaplastic ependymoma		1	1	0
II	Diffuse astrocytoma		4	1	3
II	Oligoastrocytoma		1	1	0
II	Oligodendroglioma		1	1	0
I	Pilocytic astrocytoma		2	2	0
	Sarcoma		1	1	0
	Total	111	111	55	56